Master's Thesis

Systematical Post-Synthetic Approaches to Tailoring the Structure of Metal-Organic Frameworks

Sungbin Park

Department of Chemistry

Graduate School of UNIST

2019

Systematical Post-Synthetic Approaches to Tailoring the Structure of Metal-Organic Frameworks

Sungbin Park

Department of Chemistry

Graduate School of UNIST

Systematical Post-Synthetic Approaches to Tailoring the Structure of Metal-Organic Frameworks

A thesis/dissertation
submitted to the Graduate School of UNIST
in partial fulfillment of the
requirements for the degree of
Master of Science

Sungbin Park

06. 18. 2019
Approved by

_____

Advisor
Hoi Ri Moon

Systematical Post-Synthetic Approaches to Tailoring the Structure of Metal-Organic Frameworks

Sungbin Park

This certifies that the thesis/dissertation of Sungbin Park is approved.

06. 18. 2019

_____

Advisor: Hoi Ri Moon

_____

Myoung Soo Lah

_____

Min Kim

Abstract

Metal-Organic Frameworks (MOFs), also known as Porous Coordination Polymers (PCPs) have been studied recently, in perspective of synthesis advanced structures. Since MOFs have defined structure with metal cluster and organic linkers, it is easy to modify its structures by the control in molecular level. Therefore, study about the structure of MOFs, especially in terms of, tailoring the structure of MOFs are an important issue. In this thesis, structure change, especially dimensional change of MOFs observed by Single Crystal X-Ray Diffraction (SCXRD) and core-shell MOF observed by Electron Microscopy (EM) was studied for tailoring structure *via* post-synthetic approaches.

We synthesized a MOF and transform its structure *via* radiating 365 nm wavelength of UV light. Utilized the designable property of MOFs, we chose aliphatic ligand and pillar ligand to make the 2-dimensional structure with interdigitated structure. By self-assembly of Ni(II) ion and 4-styrylpyridine (spy) and sodium form of adipate,$[Ni_2(adipate)_2(spy)_4(H_2O)_2]$ successfully synthesized. Contrast with other research, we chose adipic acid, which is an aliphatic ligand, to form a 2-dimensional layer sheet, so we could observe the dynamics when MOF changing their structure. In addition, 4-styrylpyridine successfully formed the interdigitated structure with parallel olefin bond, which can be [2+2] photodimerization by UV irradiation. Irradiation of 365 nm of UV light successfully synthesized $[Ni_2(adipate)_2(spy)_2(rctt\text{-}ppcb)(H_2O)_2]$ by cyclodimerization between two parallel olefin bond of interdigitated 4-styrylpyridine, which was monitored in Single-Crystal to Single-Crystal (SCSC) manner. Consequently, the 2-dimensional layer interdigitated structure was converted to a 3-dimensional framework. Moreover, control of irradiation time, we could obtain a partial photodimerization structure, also monitored by SCXRD.

In the second part of thesis, we also synthesized core-shell structure of MOFs *via* post-synthetic approaches. Collaborated with the simulation team, Prof. Jihan Kim at KAIST, proposed MOF on MOF core-shell structure based on their computational algorithm. As the simulation result, UiO-66 which is cubic crystal system with 12-coordination of zirconium metal in closed packed structure with terephthalate organic linkers and MIL-88B which is hexagonal crystal system with built up from the connection of trimers of iron(III) octahedra with shared μ_3-O oxygen with same organic linkers of UiO-66. In details, the {111} plane of UiO-66 and {001} plane of MIL-88B have similar cell parameter to make core-shell structure successfully. Since, UiO-66 has higher chemical and physical stability than MIL-88B, we chose UiO-66 as core MOF. In addition, in the opposite case, MIL-88B is destructed by strong acidity of $ZrCl_4$, which is precursors of UiO-66. Consequently, we use UiO-66 for core and MIL-88B epitaxially growth on the every {111} planes of UiO-66 made star-shaped

morphology of MOF successfully synthesized as a core-shell structure. Then, we expanded core-shell pairs with the isoreticular structure of UiO-66 and MIL-88B. UiO-66 with MIL-88A which is the shorter ligand than MIL-88B and MIL-88C which is the longer ligand than MIL-88B. Also, UiO-67 which is longer ligand than UiO-66 with MIL-88C. Interestingly, UiO-67 with MIL-88A and MIL-88C didn't bring up the same result with UiO-66 @MIL-88B. This will be discussed related to MOF flexibility. We also expanded cubic/cubic core-shell pair for further generalized with UiO-67@HKUST-1 pairs. The result of each core-shell synthesis was characterized by X-Ray Powder Diffraction (XRPD). The morphology and distribution of atom were defined by Scanning Electron Microscopy (SEM), Transmission Electron Microscopy (TEM), Scanning Transmission Electron Microscopy (STEM) and Energy Dispersive x-ray Spectroscopy (EDS).

Contents

List of Figures

Chapter 2

List of tables

Table 2. 4. Selected bond lengths (Å) and angles (deg.) of **2**.

Table 2. 3. Crystallographic data for [Ni(adipate)(spy)(spy0.6·½*rctt*-ppcb0.4)(H2O)] (**1'**).

Nomenclatures

MOF	Metal-organic framework
COF	Covalent-organic framework
ZIF	Zeolitic imidazolate framework
PCP	Porous coordination polymer
CP	Coordination polymer
XRPD	X-ray powder diffraction
TGA	Thermogravimetric Analysis
SEM	Scanning electron microscopy
TEM	Transmission electron microscopy
STEM	Scanning transmission electron microscopy
EDS	Energy dispersive x-ray spectroscopy
NMR	Nuclear Magnetic Resonance spectroscopy
SBU	Secondary building unit
SCSC	Single-crystal to single-crystal
CSD	Cambridge Structural Database
4-spy	4-Styryl pyridine
NDC	2,6-Naphthalene dicarboxylic acid
TEA	Triethylamine
MeOH	Methanol
EtOH	Ethanol
DMF	Dimethylformamide
BDC	Benzene-1,4,-carboxylic acid (Terephthalic acid)
BPDC	4,4’-Biphenyldicarboxylic acid
BTC	Benzene-1,3,5-tricarboxylic acid (Trimesic acid)

I. 1. General Introduction

Metal-organic Frameworks (MOFs) are a coordination-based complex composed of metal cluster and organic ligands with ordered crystalline solid compounds. These materials have exceptional porosity with a wide range of potential based on their properties such as sensing[1], hydrophilicity[2], storage[3-4], catalytic conversion[5] conductivity[6], and separation[7]. Recently, structures of MOFs attracted attention as well as functionality. The connectivity of inorganic and organic building blocks determines the structure of MOFs. The inorganic building blocks are usually metal ions or clusters called as secondary building units (SBUs).[8] The organic building units usually formed by carboxylate of anions from organic ligands. These various combinations with diverse interconnectivity make numerous structures of MOFs. Owing to these properties, the study on the structure of MOFs have been interested. Owing to well-ordered MOFs crystalline property, structures of MOFs could be utilized to advanced structures such as core-shell[9-10], dimension change[11], porous carbon[12], and glass[13] *via* post-synthetic approaches. Herein, we focused on dimensional change and hetero-structure MOFs.

Dimensional change MOFs are usually reported *via* photo-cycloaddition MOFs. There are several papers which show the dimensional change in MOFs system with partial deprotonation of ligand[14], gate adsorption properties by both solvent and vapor[15], and hydration.[16] Generally, UV induced [2+2] cycloaddition in MOFs can easily observe the dimension change owing to designing 2D MOFs is a well-known and comfortable strategy to make 3D MOFs *via* photocycloaddition. Using monodentate pillar ligand such as 4-styryl pyridine(4-spy) with various type of other organic linkers, 4-spy is well aligned with interdigitated structure facilitated by π–π interactions in the self-assembly process during crystallization[11, 17]. Moreover, Vittal et al reported 1D to 2D dimension change by UV-light in 2014 and 1D to 2D to 3D dimension change MOFs using 4-spy ligand in 2015 induced by heat and photo radiation.[18-19] Not only monodentate pillar ligand but also bidentate ligand also well aligned in 2D layer which becoming 3D framework *via* UV light.[20] In addition, solvent triggered structure change causes dimension change.[21] The merit of these dimension change is figured out by Single Crystal X-Ray Diffraction (SCXRD), so called as Single Crystal to Single Crystal transformation (SCSC) manner.[22] By doing so, the structure change with molecular movement clearly observed and visualized.[23] Moreover, SCSC transformation elucidates the details of mechanism throughout the entire reaction process.[24] In this thesis, I'll discuss dimensional change of MOFs *via* post-synthetic approaches with UV-light which observed by SCXRD. Introducing aliphatic ligand, we also observed the dynamics of ligand conformation.

The heterostructure of materials also have been explored by many researchers.[25-26] This could be the easiest way to overcoming the drawbacks of the mono-component materials. Compared with the mono-component structure, hetero-structure is more efficient, and versatile by the synergistic effect of

individual components. Two types of structure in one material have a various function such as catalyst[27], separation[28], and tandem reaction.[29] This remarkable property origin from not only their intrinsic but also extrinsic property.[30] Therefore, the study of advanced heterostructure is important to make a new class of functional materials. The easiest way to synthesize these hetero-structure materials is *via* post-synthetic approach. Among the variety of materials, MOFs is attractive material because of their crystallinity. Owing to their high crystallinity, their structure is well defined in molecular level by SCXRD. Therefore over 6,000 crystal structures have been reported to CSD (Cambridge Structural Database) and 29, 700 SCI papers have been published.[31] These databases could act as the template for heterostructure for a specific application. Therefore, many heterostructures were synthesized with MOFs, however, MOF with MOF or MOF with COF (Covalent-Organic Framework) heterostructure is rarely reported.[32-33] Owing to the rigid structure of MOF, the cell mismatching causes the failure of the heterostructure, however, herein, applying the computer simulation with database algorithm, choosing suitable two MOFs with similar cell parameter successfully make heterostructure of MOFs with core-shell structure. These phenomena will lead the new perspective of MOF field with a various combination of MOFs.

I. 2. Reference

(1) Kreno, L. E.; Leong, K.; Farha, O. K.; Allendorf, M.; Duyene, R. P. V.; Hupp, J. T. Metal-Organic Framework Materials as Chemical Sensors. *Chem. Rev.,* **2012**, *112*, 1105

(2) Chaudhari, A. K.; Mukherjee, S.; Nagarkar, S. S.; Joarder, B.; Ghosh, S. K. Bi-porous metal-organic framework with hydrophilic and hydrophobic channels: selective gas sorption and reversible iodine uptake studies. *CrystEngComm*, **2013**, *15*, 9465

(3) Sumida, K.; Rogow, D. L.; Mason, J. A.; Mcdonald, T. M.; Bloch, E. D.; Herm, Z. R.; Bae, T.-H.; Long, J. R. Carbon Dioxide Capture in Metal-Organic Frameworks. *Chem. Rev.,* **2012**, *112*, 724

(4) Suh, M. P.; Park, H. J.; Prasad, T. K.; Lim, D.-W. Hydrogen Storage in Metal-Organic Frameworks. *Chem. Rev.,* **2012**, *112*, 782

(5) Phan, A.; Czaja, A. U.; Gándara, F.; Knobler, C. B.; Yaghi, O. M. Metal-Organic Frameworks of Vanadium as Catalysts for Conversion of Methane to Acetic Acid. *Inorg, Chem.,* **2011**, *50*, 7388

(6) Sheberla, D.; Bachman, J. C.; Elias, J. S.; Sun, C.-J.; Horn, Y. S.; Dincă, M. Conductive MOF electrodes for stable supercapacitors with high areal capacitance. *Nat. Mater.,* **2017**, *16*, 220

(7) Li, J.-R.; Sculley, J.; Zhou, H.-C. Metal-Organic Frameworks for separations. *Chem. Rev.*, **2012**, *112*, 869

(8) Kim, D.; Liu, X.; Lah, M. S. Topology analysis of metal-organic frameworks based on metal-organic polyhedral as secondary or tertiary building units. *Inorg. Chem. Front.,* **2015**, *2*, 336

(9) Koh, K.; Wong-Foy, A. G.; Matzger, A. J. MOF@MOF: microporous core-shell architectures. *Chem. Commun.,* **2009**, *0*, 6162

(10) Tang, J.; Salunkhe, R. R.; Liu, J.; Torad, N. L.; Imura, M.; Furukawa, S.; Yamauchi, Y. Thermal Conversion of Core-Shell Metal-Organic Frameworks: A New Method for Selectively Functionalized Nanoporous Hybrid Carbon. *J. Am. Chem. Soc.,* **2015**, *137*, 1572

(11) Medishetty, R.; Tandiana, R.; Koh, L. L.; Vittal, J. J. Assembly of 3D Coordination Polymers from 2D Sheets by [2+2] Cycloaddition Reaction. *Chem. Eur. J.*, **2014**, *20*, 1231

(12) Jeoung, S.; Ju, I. T.; Kim, J. H.; Joo, S. H.; Moon, H. R. Hierarchically porous adamantane-shaped carbon nanoframes. *J. Mater. Chem. A.*, **2018**, *6*, 18906

(13) Zhou, C.; Longley, L.; Krajnc, A.; Smales, G. J.; Qiao, A.; Erucar, I.; Doherty, C. M.; Thornton, A. W.; Hill, A. J.; Ashling, C. W.; Qazvini, O. T.; Lee, S. J.; Chater, P. A.; Terrill, N. J.; Smith, A. J.; Yue, Y.; Mali, G.; Keen, D. A.; Telfer, S. G.; Bennett, T. D. Metal-organic framework glasses with permanent accessible porosity. *Nat. Commun.*, **2018**, *9*, 5042

(14) Mu, B.; Li, F.; Walton, K. S. A novel metal-organic coordination polymer for selective adsorption of CO_2 over CH_4. *Chem. Commun.*, **2009**, *0*, 2493

(15) Kondo, A.; Suzuki, T.; Kotani, R.; Maeda, K. Liquid/vapor-induced reversible dynamic structural transformation of a three-dimensional Cu-based MOF to a one-dimensional MOF showing gate adsorption. *Dalton Trans.*, **2017**, *46*, 6762

(16) Cheng, Y.; Kondo, A.; Noguchi, H.; Kajiro, H.; Urita, K.; Ohba, T.; Kaneko, K.; Kanoh, H. Reversible Structural Change of Cu-MOF on Exposure to Water and Its CO_2 Adsorptivity. *Langmuir*, **2009**, *25*, 4510

(17) Medishetty, R.; Park, I.-H.; Lee, S. S.; Vittal, J. J.; Solid-state polymerization *via* [2+2] cycloaddition reaction involving coordination polymers. *Chem. Commun.*, **2016**, *52*, 3989

(18) Medishetty, R.; Husain, A.; Bai, Z.; Runčevski, T.; Dinnebier, R. E.; Naumov, P.; Vittal, J. J. Single Crystals Popping Under UV Light: A Photosalient Effect Triggered by a [2+2] Cycloaddition Reaction. *Angew. Chem.*, **2014**, *126*, 6017

(19) Medishetty, R.; Tandiana, R.; Wu, J.; Bai, Z.; Du, Y.; Vittal, J. J. A Step-by-Step Assembly of a 3D Coordination Polymer in the Solid-State by Desolvation and [2+2] Cycloaddition Reactions. *Chem. Eur. J.*, **2015**, *21*, 11948

(20) Park, I.-H.; Medishetty, R.; Lee, S. S.; Vittal, J. J. Solid-state polymerization in a polyrotaxane coordination polymer *via* a [2+2] cycloaddition reaction. *Chem. Commun.,* **2014**, *50*, 6585

(21) Claassens, I. E.; Nikolayenko, V. I.; Haynes, D. A.; Barbour, L. J. Solvent-Mediated Synthesis of Cyclobutane Isomers in a Photoactive Cadmium(II) Porous Coordination Polymer. *Angew. Chem., Int. Ed.,* **2018**, *57*, 15563

(22) Ito, H.; Muromoto, M.; Kurenuma, S.; Ishizaka, S.; Kitamura, N.; Sat, H.; Seki, T. Mechanical stimulation and solid seeding trigger single-crystal-to-single-crystal molecular domino transformations. *Nat. Commun.,* **2013**, *4*, 2009;

(23) Chaudhary, A.; Mohammad, A.; Mobin, S. M. Recent Advances in Single-Crystal-to-Single-Crystal Transformation at the Discrete Molecular Level. *Cryst. Growth Des.,* **2017**, *17*, 2893

(24) Huang, S.-L.; Hor, T. S. A.; Jin, G.-X. Photodriven single-crystal-to-single-crystal transformation. *Coord. Chem. Rev.,* **2017**, *346*, 112

(25) Song, X.; Kim, T. K.; Kim, H.; Kim, D.; Jeong, S.; Moon, H. R.; Lah, M. S. Post-Synthetic Modifications of Framework Metal Ions in Isostructural Metal-Organic Frameworks: Core-Shell Heterostructures *via* Selective Transmetalations. *Chem. Mater.,* **2012**, *24*, 3065

(26) Szilágyi, P. Á.; Lutz, M.; Gascon, J.; Juan-Alcañiz, J.; Esch, J. v.; Kapteijn, F.; Geerlings, H.; Dam, B.; Krol, R. v. d. MOF@MOF core-shell *vs.* Janus particles and the effect of strain: potential for guest sorption, separation and sequestration. *CrystEngComm,* **2013**, *15*, 6003

(27) Ma, T. Y.; Dai, S.; Jaroniec, M.; Qiao, S, Z. Metal-Organic Framework Derived Hybrid Co_3O_4-Carbon Porous Nanowire Arrays as Reversible Oxygen Evolution Electrodes. *J. Am. Chem. Soc.,* **2014**, *136*, 13925

(28) Wang, D.; He, J.; Rosenzweig, N.; Rosenzweig, Z. Superparamagnetic Fe_2O_3 Beads-CdSe/ZnS Quantum Dots Core-Shell Nanocomposite Particles for Cell Separation. *Nano Lett.,* **2004**, 4, 409

(29) Shaner, M. R.; Fountaine, K. T.; Ardo, S.; Coridan, R. H.; Atwater, H. A.; Lewis, N. S. Photoelectrochemistry of core-shell tandem junction n-p^{+}-si/n-WO_3 microwire array photoelectrodes. *Energy Environ. Sci.*, **2014**, *7*, 779

(30) Ruf, T.; Repp, S.; Urban, J.; Thomann, R.; Erdem, E. Competing effects between intrinsic and extrinsic defects in pure and Mn-doped ZnO nanocrystals. *J Nanopart Res.*, **2016**, *18*, 109

(31) Furukawa, H.; Cordova, K. E.; O'Keeffe, M.; Yaghi, O. M. The Chemistry and Applications of Metal-Organic Frameworks. *Science*, **2013**, *341*, 1230444

(32) Kim, D.; Lee, G.; Oh, S.; Oh, M. Unbalanced MOF-on-MOF growth for the production of a lopsided core-shell of MIL-88B@MIL-88A with mismatched cell parameters. *Chem. Commun.*, **2019**, *55*, 43

(33) Sun, D.; Jang, S.; Yim. S.-J.; Ye, L.; Kim, D.-P. Metal Doped Core-Shell Metal-Organic Frameworks@Covalent Organic Frameworks (MOFs@COFs) Hybrids as a Novel Photocatalytic Platform. *Adv. Funct. Mater.*, **2018**, *28*, 17901190

II. Dimensional change of Metal-Organic Framework : SCSC transformation

II. 1. Introduction

Solid-state photoreactions have attracted increasing attention as an environmentally benign approach on account of their solvent-less procedure.[1-2] In particular, in a crystalline phase these reactions are expected to be selective and efficient, because the photoreactive species are regularly arranged in view of distances and geometries.[3-4] [2 + 2] photodimerization of a pair of olefins is a well-known reaction that occurs in the solid state, in which the traditional solution synthesis hardly affords the products, cyclobutane moieties.[5] The pioneering work done by Schmidt et al. showed that the potentially reactive olefin pairs should be located less than ca. 4.2 Å apart, called Schmidt's criteria,[6] as shown in Figure. 2. 1. In order to achieve well-aligned double bonds in crystals, various strategies have been employed so far. These strategies include co-crystallization templated by hydrogen bonds,[7-8] π–π stacking[9-10] or halogen bonding,[11] coordination-driven metal–organic assemblies,[12-14] inclusion of guest molecules in the host cavity,[15-16] and utilization of substituted functional groups to assist the stereoselective arrangement of the olefin pairs.[17-18]

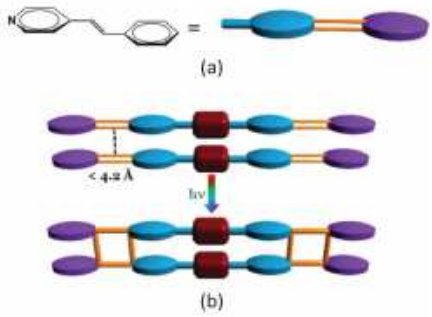

Figure 2. 1. (a) A typical monodentate ligand containing an olefin bond. (b) 'Face-to-face' olefin bond pairs in the packing of metal complexes within 4.2 **Å**. The cherry red object represents the metal ions.

Coordination polymers (CPs) and metal-organic frameworks (MOFs) have been utilized as platforms for solid-state photoreactions due to their ease of structural tunability and functionality.[19-20] Olefin-containing ligands and guest molecules, if present, can be well-positioned and oriented in the framework or pores so as to react upon UV-irradiation.[21–24] The [2 + 2] cycloaddition reaction has been intensively studied by triggering the UV-induced regio- and stereoselective dimerization and polymerization with the intermolecular olefin bond pairs in the MOF system. For example, Vittal and Lee's group presented a 1D CP fused with an unusual organic polymer ligand synthesized by the photopolymerization of a six-folded interpenetrated MOF in Figure 2. 2, and Figure 2. 3.[23]

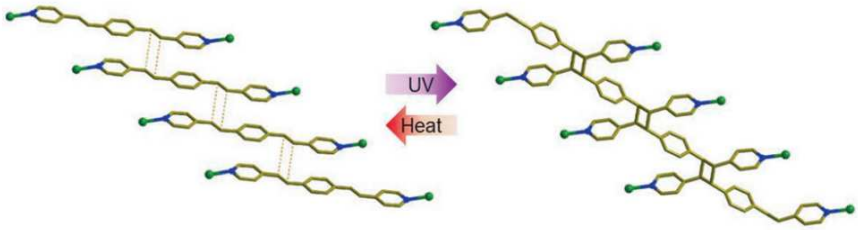

Figure 2. 2. Reversible polymerization by [2+2] photo-cycloaddition of slip-stacked bpeb ligands in a MOF and depolymerization of the resultant poly-cyclo-butanes. Both processes occur through SCSC transformations.

Figure 2. 3. The six-fold interpenetration MOF, with channels along the *c*-axis

Kitagawa et al. reported the employment of [2 + 2] cycloadditions in a MOF synthesis to fine-tune the nanopores and verify the mechanism of their adsorbate-selective gate effect.[24] (Figure 2. 4.)

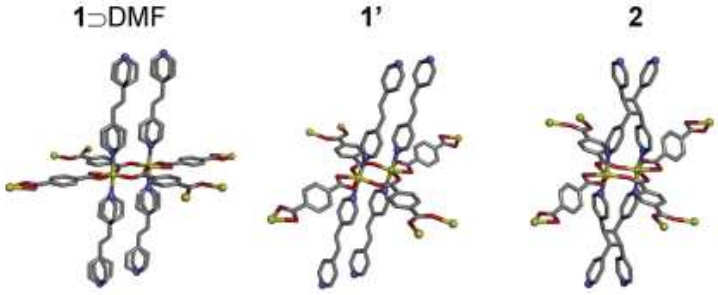

Figure 2. 4. Crystal structure of MOF. Colour scheme: Mn, yellow; O, red; N, blue; C, gray. **1⊃DMF** represented solvated MOF, **1'** represented desolvated MOF of **1**, **2** represented [2+2] photodimerization of olefin bonds of **1'**.

Moreover, photoinduced post synthetic modification of pore size *via* host-guest cycloaddition reaction in a MOF system lead CO_2 selectivity performance is reported by Hazra et al.[25] (Figure 2. 5.)

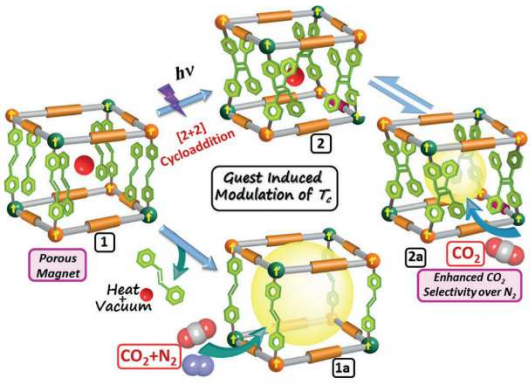

Figure 2. 5. Schematic diagram of photoinduced post synthetic modification of MOF

Recently, solvent-mediated synthesis of cyclobutane isomers in a MOF system also studied by Claasens et al. Well stacked 2D layers change inter- and intra- distance of olefin bonds induced not only cyclobutane isomers, but also change the whole MOF dimension.[26] (Figure 2. 6.)

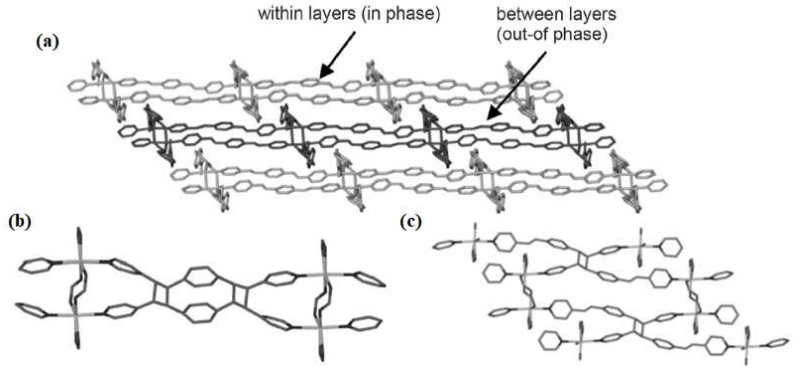

Figure 2. 6. (a) Schematic diagram of stacked 2D layer structure of MOF. (b) Cycloaddition of olefin bonds within layers. (in phase) (c) Cycloaddition of olefin bonds between layer (out-of phase) change MOF dimension from 2D to 3D.

Herein, to construct the photoreactive crystalline CP, we employ a mixed-ligand system of an olefin-containing ligand, 4-styrylpyridine (spy), and adipate as a flexible linker with Ni(II) ions.[27] Upon UV-irradiation, the as-synthesized 2-dimensional (2D) CP is converted to a 3-dimensional (3D) CP through the cycloaddition reaction, which is monitored in a single-crystal-to-single-crystal (SC–SC) manner to provide direct structural information about the reaction progress. Interestingly, the severe strain originating from the atomic dislocations during the reaction can be released by the conformational change of the adipate ligands.

II. 2. Experiment Section

Materials and Methods.

All chemicals and solvents were reagent grade and used without further purification. Elemental analyses were performed at the UNIST Central Research Facilities Center (UCRF) in Ulsan National Institute of Science and Technology (UNIST). Thermogravimetric analysis (TGA) were performed under N_2(g) atmosphere at a scan rate of 1 ℃ min^{-1} using Q50 from TA instruments. IR spectra were recorded with a ThermoFisher Scientific Nicolet 6700 FT-IR spectrophotometer. X-ray powder diffraction (XRPD) data were recorded on a Bruker D2 phaser diffractometer at 30 kV and 10 mA for Cu Kα (λ = 1.541 Å), with a step size of 0.02º in 2θ. Nuclear magnetic resonance (NMR) spectra were recorded on a Agilent 400-MR DD2 spectrometer.

Synthesis of [Ni(adipate)(4-spy)$_2$(H_2O)] (1)

$Ni(NO_3)_2$•$6H_2O$ (29.3 mg, 0.1 mmol) and the sodium adipate (19 mg, 0.1 mmol) were dissolved in a mixture of ethanol and water with volume ratio of 2 mL:1 mL and 1 mL:2mL respectively. The solution of $Ni(NO_3)$•$6H_2O$ was diffused onto the latter solution. Subsequently, a methanol solution (3 mL) of 4-styrylpyridine (4-spy) (18 mg, 0.1 mmol) were carefully added. The mixture solution allowed to stand at room temperature for 7 days until the green crystals were fully synthesized. Yield : 64 %. Anal. Calcd for $Ni_1C_{32}H_{32}N_2O_5$: C, 63.83; H, 5.49; N, 4.80.; Found: C, 64.51; H, 5.50; N, 4.78

Synthesis of single crystlas of [Ni(adipate)(rctt-ppcb)(4-spy)$_2$(H_2O)$_2$] (2) from 1

After UV irradiation (365 nm, 0.7 klx by Hg lamp) of **1** for 24 h, green crystals of [Ni(adipate)(rctt-ppcb)(4-spy)$_2$(H_2O)$_2$] **(2)** (rctt-ppcb = *regio-cis, trans, trans*-1,3-bis(4'-pyridyl)-2,4-bis(phenyl)(cyclobutane) were obtained. Anal. Calcd for $Ni_1C_{32}H_{32}N_2O_5$: C, 63.83; H, 5.49; N, 4.80.; Found: C, 64.34; H, 5.35; N, 4.79

Preparation of the bulk powder sample of 2

For preparation, the crystals of **1** were ground in powder form, and thinly spread onto the glass substrate. Upon the UV-irradiation (365 nm, 1.2 klx by Hg lamp), the bulk samples of **2** (6 h) and **1'** (1 h) was synthesized.

Single-crystal X-ray crystallography

Single crystals of **1, 2**, and **1'** were coated with paratone-*N* oil, and the diffraction data were measured at 100 K with synchrotron radiation (λ = 0.63000, 0.70000, and 0.70000 Å, respectively) on an ADSC Quantum-210 detector at 2D SMC with a silicon (111) double crystal monochromator (DCM) at the Pohang Accelerator Laboratory, Republic of Korea. The ADSC Q210 ADX program[30] were used for data collection, and HKL3000sm (Ver. 730r)[31] were used for cell refinement, reduction, and absorption correction. The crystal structures were solved by direct methods with SHELX-XS (Ver. 2014/5)[32] and refined by full-matrix least-squares calculations with SHELX-XL (Ver. 2014/7)[33]. All non-hydrogen atoms in whole structures were refined anisotropically. A summary of the crystals and some crystallographic data are given in Table 1-6. CCDC 1524563 (**1**), CCDC 1524564 (**2**), and CCDC 1524565 (**1'**) contain the supplementary crystallographic data for this paper. The data can be obtained free of charge at www.ccdc.cam.ac.uk/conts/retrieving.html or from the Cambridge Crystallographic Data Centre, 12, Union Road, Cambridge CB2 EX, UK.

II. 3. Result and Discussion

The self-assembly of $Ni(NO_3)_2 \cdot 6H_2O$, sodium adipate, and spy yielded green crystals of $[Ni(adipate)(spy)_2(H_2O)]$ **(1)** (see experimental for details). **CP 1** crystallizes in the monoclinic space group $P2_1/n$ and is composed of 2D coordination networks stacked in an interdigitated fashion (Figure 2. 7.).

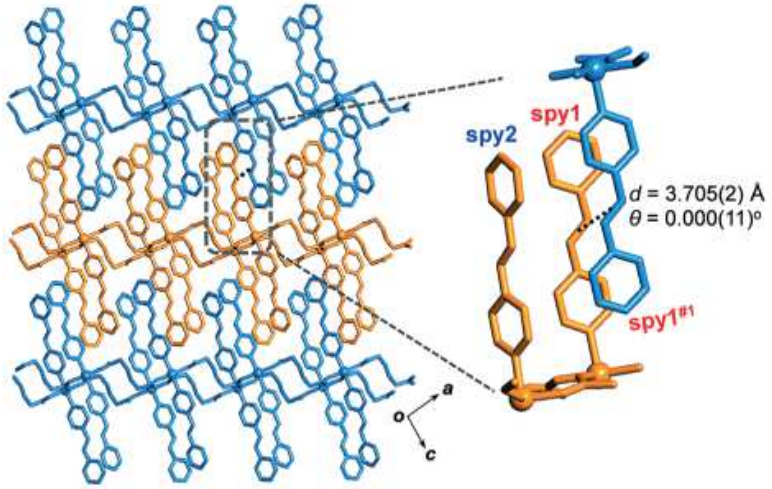

Figure 2. 7. The crystal structure of **CP 1** with distance (*d*) and dihedral angle (θ) between double bonds in spy ligands from two different layers.

The asymmetric unit of **1** contains one octahedral Ni(II) ion, two spy and one adipate ligands, and one coordinating water molecule (Figure. 2. 8. and Table 2. 1.).

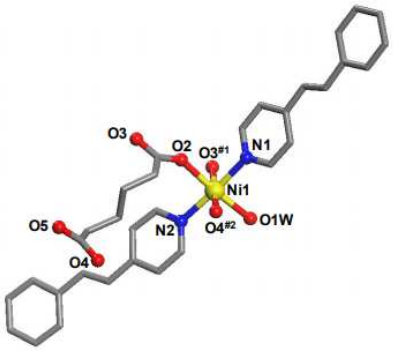

Figure 2. 8. An assymetric unit of **1**. Symmetry operations: #1, -x+1/2, 6+1/2, -z+1/2, #2, -x+1, -y+1, -z+1 x

Table 2. 1. X-ray crystallographic data of [Ni(adipate)(spy)$_2$(H$_2$O)] (**1**).

Empirical formula	C32 H32 N2 O5 Ni
Formula weight	583.30
Temperature	100(2) K
Wavelength	0.63000 Å
Crystal system	Monoclinic
Space group	$P2_1/n$
Unit cell dimensions	a = 18.788(4) Å
	b = 8.3400(17) Å
	c = 18.868(4) Å
	α = 90°
	β =115.53(3) °
	γ =90°
Volume^3	2696.6(11) Å
Z	4
Density (calculated)	1.437 g cm^{-3}
Absorption coefficient (μ)	0.552 mm^{-1}
F(000)	1114
θ range for data collection	1.797 to 33.355°
Index ranges	-32<=h<=32, -14<=k<=14, -32<=l<=32
Reflections collected	40553
Independent reflections	12624 [R(int) = 0.0660]
Completeness to θ = 28.00°	99.7 %
Refinement method	Full-matrix least-squares on F^2
Data / restraints / parameters	12624 / 0 / 369
Goodness-of-fit on F^2	0.975
R_1[a] , wR_2[b] [I>2σ(I)]	0.0406, 0.1008
R_1[a] , wR_2[b] (all data)	0.0683, 0.1107
Largest diff. peak and hole	0.677 and -1.299 e.Å-3

[a]$R = \Sigma||F_o| - |F_c||/\Sigma|F_o|$. [b]$wR(F^2) = [\Sigma w(F_o^2 - F_c^2)^2 / \Sigma w(F_o^2)^2]^{1/2}$ where $w = 1/[\sigma^2 (F_o^2) + (0.0632P)^2 + (0.00)P]$, $P = (F_o^2 + 2F_c^2)/3$.

Ni(II) ions are coordinated by one water molecule and three oxygen atoms of carboxylate anions from three different adipate ligands to construct the 2D layered structure in the (−101) plane (Figure. 2. 9.).

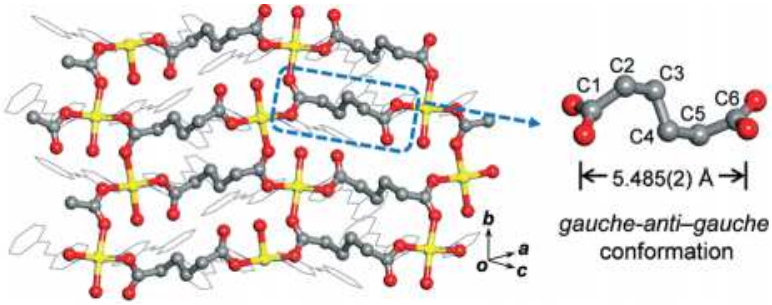

Figure 2. 9. Top view of the Ni-adipate layer and the conformation of the adipate ligand. colour scheme: Ni : yellow; C, grey; O, red; N, blue)

Among the four O atoms of an adipate ligand, three O atoms participate in the coordination in the monodentate mode, and thus the ligand acts as a 3-connected node. The spy ligands occupying the apical sites of Ni(II) are vertically projected from the basal plane, which makes each 2D sheet packed in an interdigitated manner. The adjacent spy ligands from the adjacent layers show strong π–π interactions between their aromatic rings (range of adjacent C···C distances = 3.547–4.575 Å). As highlighted in Figure. 2. 7, between the two crystallo-graphically independent spy ligands (spy1 and spy2), only spy1 ligands have a pair of olefin bonds surpassing Schmidt's requirement to undergo the [2 + 2] cycloaddition reaction as the pairs are aligned parallel with a distance of 3.705(2) Å. Particularly, the photoreactive spy1 ligands are aligned in a head-to-tail manner derived from the two neighbouring sheets. This presents the opportunity for a structural transformation from 2D to 3D upon successful photodimerization. The conformation of the adipate ligand is worthy of attention as it has a gauche–anti–gauche conformation [torsion angle C1–C2–C3– C4 = −74.48(14)°; torsion angle C2–C3–C4–C5 = 177.21(10)°; torsion angle C3–C4–C5–C6 = 58.39(15)°; chain length C1···C6 = 5.485(2) Å] (highlighted in Fig. 2. 7.). The conformational change of this flexible ligand is an important feature of the present CP system to retain the single crystallinity upon the photodimerization as it will be discussed further.

Irradiation with UV light (365 nm) for 24 h on the single-crystals of **1** resulted in a [2 + 2] cycloaddition of the olefin pairs, generating $[Ni_2(adipate)_2(spy)_2(rctt\text{-}ppcb)(H_2O)_2]$ (**2**; rctt-ppcb = regio-cis,trans,trans-1,3-bis(4′-pyridyl)-2,4-bis(phenyl)cyclobutane) by the SC–SC transformation. The single-crystal X-ray diffraction (SCXRD) analysis clearly shows the formation of cyclobutane rings that originate from the olefin bond pairs of the spy1 ligands in 1, bridging its sheets to afford the 3D framework (Figure 2. 10. and Table 2. 2.).

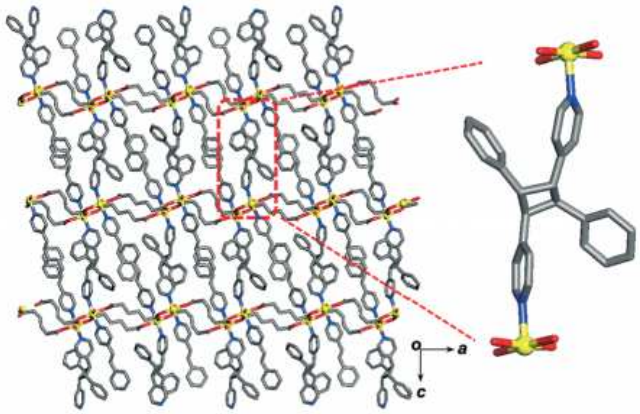

Figure 2. 10. The crystal structure of **CP 2**.

Table 2. 2. Crystallographic data for $[Ni_2(adipate)_2(spy)_2(rctt\text{-}ppcb)(H_2O)_2]$ (**2**).

Empirical formula	C64 H64 N4 O10 Ni2
Formula weight	1166.61
Temperature	100(2) K
Wavelength	0.70000 Å
Crystal system	Monoclinic
Space group	$P2_1/c$
Unit cell dimensions	a = 21.305(4) Å
	b = 8.5080(17) Å
	c = 30.830(6) Å
	α = 90°
	β = 94.27(3)°
	γ = 90°
Volume	5575(2) $Å^3$
Z	4
Density (calculated)	1.390 g cm^{-3}
Absorption coefficient (μ)	0.708 mm^{-1}
F(000)	2448
θ range for data collection	1.552 to 33.270°.
Index ranges	-33<=h<=33, -12<=k<=12, -47<=l<=47
Reflections collected	34671
Independent reflections	18478 [R(int) = 0.0431]
Completeness to θ = 28.00°	98.1 %
Refinement method	Full-matrix least-squares on F^2
Data / restraints / parameters	18478 / 101 / 851
Goodness-of-fit on F^2	1.010
$R_1{}^a$, $wR_2{}^b$ [$I>2\sigma(I)$]	0.0774, 0.2061
$R_1{}^a$, $wR_2{}^b$ (all data)	0.1578, 0.2500
Largest diff. peak and hole	1.459 and -1.153 e.$Å^{-3}$

$^a R = \Sigma||F_O| - |F_C||/\Sigma|F_O|$. $^b wR(F^2) = [\Sigma w(F_O{}^2 - F_C{}^2)^2/\Sigma w(F_O{}^2)^2]^{1/2}$ where $w = 1/[\sigma^2(F_O{}^2) + (0.1424P)^2 + (0.00)P]$, $P = (F_O{}^2 + 2F_C{}^2)/3$.

On the other hand, the photo-inactive spy2 remained intact after the photoreaction, dangling on the layer in **CP 2**. During the transformation from **1** to **2**, the space group changed from $P2_1/n$ to $P2_1/c$ with the asymmetric unit containing two Ni(II) ions, two spy, two adipate, one rctt-ppcb, and two water molecules, which are quantitatively twice that of 1 due to reduced symmetry (Figure 2. 11.).

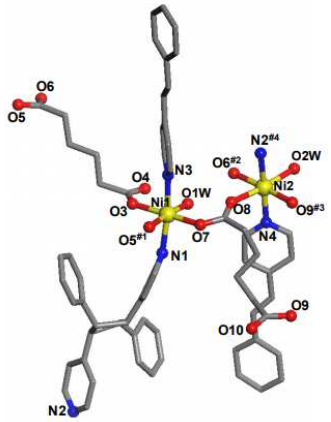

Figure 2. 11. An asymmetric unit of **2**. Disordered parts are omitted for clarity. Symmetry operations: #1, -x+1, -y+2, -z+2; #2, -x+1, -y+1, -z+2; #3, -x, -y+1, -z+2; #4, x, -y+3/2, z+1/2.

In the structure of **2**, one adipate, one spy, and a phenyl ring of rctt-ppcb are disordered, which are described in Figure. 2. 12.

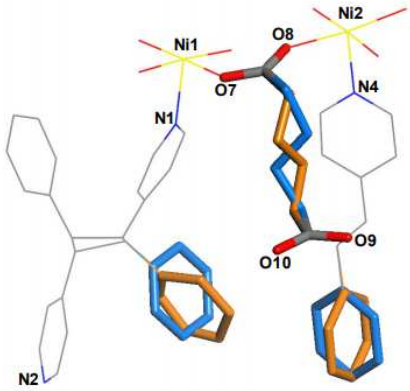

Figure 2. 12. Disorders observed in **2**: one adipate, a phenyl ring of a spy ligand, and a phenyl ring of rctt-ppcb.

In the CP or MOF system, several interesting examples of dimensional changes of the structures upon photodimerization have been reported.[32-36] Vittal et al. reported a solid-state transformation from a 2D CP into a 3D interpenetrated structure by the [2 + 2] cycloaddition of 4-styrylpyridine.[35](Figure 2. 13. (a)) Tong and his co-workers also reported a transformation from 1D to 3D by using staggered-sculls chains.[36] (Figure 2. 13 (b))

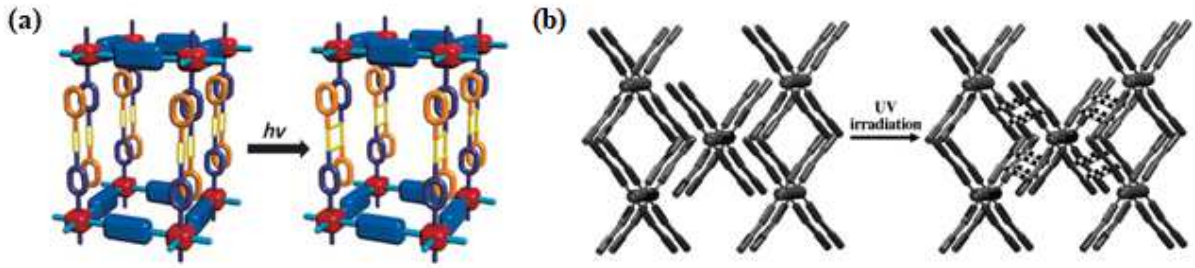

Figure 2. 13. (a) Schematic diagram of MOF, Vittal et al. (b) schematic diagram of MOF, Tong et al.

Along with these, the present system can be a good example of constructing high dimensional crystal structures by crystal engineering in the solid-state by a photoreaction.

Despite the four-membered ring formation, the octahedral geometry of Ni(II) ions was intact as in 1 with a slight change of the angles around them (Tables 2. 3 and 4). However, the dynamic atomic displacements in the ligand side for adipate and spy were more severe: (1) the geometry change of π–π interactions for some aromatic rings, and (2) the conformational change of adipate. In **2**, the aromatic units of spy and rctt-ppcb ligands still exhibit strong π–π interactions (range of adjacent C···C distances = 3.414–4.595 Å).

Table 2. 3. Selected bond lengths (Å) and angles (deg.) of **1**.

Ni(1)-O(1)	2.0438(10)	Ni(1)-O(2)	2.0664(10)
Ni(1)-O(3)$^{\#1}$	2.0779(12)	Ni(1)-O(4)$^{\#2}$	2.0923(12)
Ni(1)-N(1)	2.1017(11)	Ni(1)-N(2)	2.1103(11)
O(1)-Ni(1)-O(2)	175.57(4)	O(1)-Ni(1)-O(3)$^{\#1}$	96.83(4)
O(2)-Ni(1)-O(3)$^{\#1}$	80.82(4)	O(1)-Ni(1)-O(4)$^{\#2}$	87.31(4)
O(2)-Ni(1)-O(4)$^{\#2}$	94.92(4)	O(3)$^{\#1}$-Ni(1)-O(4)$^{\#2}$	175.44(4)
O(1)-Ni(1)-N(1)	88.75(4)	O(2)-Ni(1)-N(1)	87.37(4)
O(3)$^{\#1}$-Ni(1)-N(1)	86.81(5)	O(4)$^{\#2}$-Ni(1)-N(1)	91.40(5)
O(1)-Ni(1)-N(2)	94.74(4)	O(2)-Ni(1)-N(2)	89.06(4)
O(3)$^{\#1}$-Ni(1)-N(2)	90.62(5)	O(4)$^{\#2}$-Ni(1)-N(2)	90.93(5)
N(1)-Ni(1)-N(2)	175.89(4)		

Symmetry transformations used to generate equivalent atoms:

#1 -x+1/2,y+1/2,-z+1/2 #2 -x+1,-y+1,-z+1 #3 -x+1/2,y-1/2,-z+1/2

Table 2. 4. Selected bond lengths (Å) and angles (deg.) of **2**.

Ni(1)-O(7)	2.043(2)	Ni(1)-O(3)	2.055(3)
Ni(1)-O(1)	2.059(2)	Ni(1)-O(5)$^{\#1}$	2.062(2)
Ni(1)-N(3)	2.113(3)	Ni(1)-N(1)	2.137(3)
Ni(2)-O(2)	2.053(2)	Ni(2)-O(8)	2.056(2)
Ni(2)-O(6)$^{\#2}$	2.064(2)	Ni(2)-O(9)$^{\#3}$	2.071(3)
Ni(2)-N(2)$^{\#4}$	2.105(3)	Ni(2)-N(4)	2.110(3)
O(7)-Ni(1)-O(3)	175.61(9)	O(7)-Ni(1)-O(1)	95.88(10)
O(3)-Ni(1)-O(1)	88.43(10)	O(7)-Ni(1)-O(5)$^{\#1}$	80.22(9)
O(3)-Ni(1)-O(5)$^{\#1}$	95.50(9)	O(1)-Ni(1)-O(5)$^{\#1}$	175.30(10)
O(7)-Ni(1)-N(3)	92.55(11)	O(3)-Ni(1)-N(3)	86.46(11)
O(1)-Ni(1)-N(3)	92.44(10)	O(5)$^{\#1}$-Ni(1)-N(3)	90.37(9)
O(7)-Ni(1)-N(1)	93.45(11)	O(3)-Ni(1)-N(1)	87.44(11)
O(1)-Ni(1)-N(1)	88.49(10)	O(5)$^{\#1}$-Ni(1)-N(1)	89.12(10)
N(3)-Ni(1)-N(1)	173.80(12)	O(2)-Ni(2)-O(8)	174.01(10)
O(2)-Ni(2)-O(6)$^{\#2}$	95.04(10)	O(8)-Ni(2)-O(6)$^{\#2}$	80.79(9)
O(2)-Ni(2)-O(9)$^{\#3}$	88.51(10)	O(8)-Ni(2)-O(9)$^{\#3}$	95.68(9)
O(6)$^{\#2}$-Ni(2)-O(9)$^{\#3}$	176.44(9)	O(2)-Ni(2)-N(2)$^{\#4}$	88.62(10)
O(8)-Ni(2)-N(2)$^{\#4}$	87.12(10)	O(6)$^{\#2}$-Ni(2)-N(2)$^{\#4}$	90.62(11)
O(9)$^{\#3}$-Ni(2)-N(2)$^{\#4}$	89.68(12)	O(2)-Ni(2)-N(4)	94.41(10)
O(8)-Ni(2)-N(4)	89.95(9)	O(6)$^{\#2}$-Ni(2)-N(4)	90.47(11)
O(9)$^{\#3}$-Ni(2)-N(4)	89.04(11)	N(2)$^{\#4}$-Ni(2)-N(4)	176.67(10)

Symmetry transformations used to generate equivalent atoms:

#1 -x+1,-y+2,-z+2 #2 -x+1,-y+1,-z+2 #3 -x,-y+1,-z+2
#4 x,-y+3/2,z+1/2

Meanwhile, the two phenyl rings of rctt-ppcb indicate the change of their π–π interaction geometry with another phenyl ring of spy from the offset face-to-face interaction to the edge-to-face interaction as a result of photodimerization (Figure 2. 14.); in 1 the shortest C···C distance was 3.803 Å and the dihedral angle was 15.23°, whereas in 2 it was 3.629 Å and 43.03° for a ring pair and 3.634 Å and 96.48° for the other one. For the adipate ligands, the conformational changes are observed during the photochemical transformation. Between the two crystallographically different adipate ligands, one has an anti–anti– anti conformation [torsion angle C1–C2–C3–C4 = −172.6(3)°; torsion angle C2–C3–C4–C5 = 178.6(3)°; torsion angle C3–C4– C5–C6 = 170.2(3)°; chain length C1···C6 = 6.283(5) Å] and the other has a gauche–anti–gauche conformation [torsion angle C7–C8A–C9A–C10A = 58.6(10)°; torsion angle C8A–C9A–C10A– C11A = 174.2(9)°; torsion angle C9A–C10A–C11A–C12 = 77.7(11)°; chain length C7···C12 = 5.392(5) Å]. Overall, the distance between the 2D networks has been shortened from 15.93 Å to 15.37 Å, but the volume slightly increased by 3% because of the extension along the 2D layers. This implies that the surrounding molecules are collectively and dynamically moved upon formation of cyclobutane in order to stabilize the whole framework.

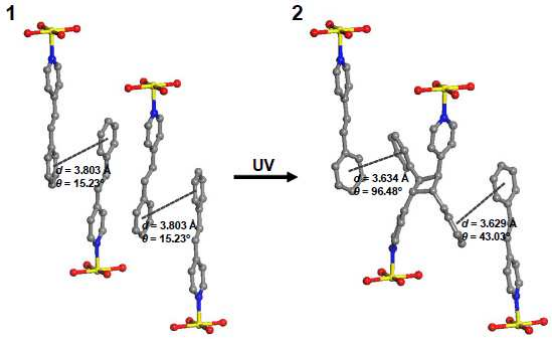

Figure 2. 14. The geometrical change of π–π interactions with the phenyl rings, from the offset face-to-face interaction in **1** to the edge-to-face interaction in **2.**

By controlling the irradiation time (6 h), we could obtain the partially photodimerized compound [Ni(adipate)(spy)($spy_{0.6}$·½rctt-$ppcb_{0.4}$)(H_2O)] (**1′**) (Table 2. 5.), which provides direct structural information about the reaction progress. As determined by the SCD analysis, **1′** is isostructural to **1** except for the formation of rctt-ppcb observed as a disorder (Figure. 2. 15.), which has an occupancy ratio of 40% to spy.

Figure 2. 15. The crystal structure of CP **1'** produced by the partial photodimerization reaction of **1**. (reactant phase : product phase = 0.602 : 0.98)

In this structure, the conformation of adipate remains the same as that in **1**, contrary to what was observed in **2**. The cyclobutane rings in **1′** show a centrosymmetric planar conformation [cyclobutane torsion = 0.0(8)°]. This is clearly distinguishable from the cyclobutane species in **2**, which has a puckered conformation with a torsion angle of 11.6(1)° (Figure 2. 16.). In general, the coplanar cyclobutane has a higher strain energy by approximately 110 kJ mol^{-1} compared with the puckered form,[37] which means that the energy is accumulated in the crystal as the photodimerization progresses to completion. Therefore, in order to stabilize the final structure, the conformational change of cyclobutane occurred along with the geometrical change of π–π interactions as well as the conformational motions of adipate.

The XRPD studies (Figure 2. 17.) show that the photo-transformation for the bulk powder sample is completed within 6 h upon UV-irradiation whose light power is ca. 1.2 klx. The XRPD patterns of **1** and **2** match well with the (hkl) reflections simulated from the SCD data, respectively, which confirms the successful structural change from bulk **1** to **2** as well as the purity of the samples. The peak related to the d-spacing ((10– 1) for **1** and (002) for **2**) between the layers is shifted to a higher angle from 5.52° to 5.78° because of its contraction as previously mentioned.

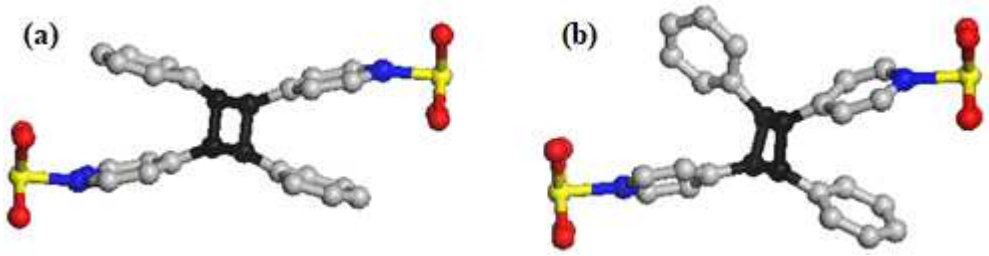

Figure 2. 16. (a) Planar conformation cyclobutane of **1',** (b) puckered conformation cyclobutene of **2.** Black coloured atom highlighted cyclobutene and disorder is omitted for clarity.

Table 2. 5. Crystallographic data for [Ni(adipate)(spy)(spy$_{0.6}$·½*rctt*-ppcb$_{0.4}$)(H$_2$O)] (**1'**).

Empirical formula	C32 H32 N2 O5 Ni
Formula weight	583.30
Temperature	100(2) K
Wavelength	0.65000 Å
Crystal system	Monoclinic
Space group	$P2_1/n$
Unit cell dimensions	a = 18.732(4) Å
	b = 8.4040(17) Å
	c = 18.827(4) Å
	α = 90°
	β = 115.03(3)°
	γ = 90°
Volume	2685.5(11) Å^3
Z	4
Density (calculated)	1.443 g cm^{-3}
Absorption coefficient (μ)	0.603 mm^{-1}
F(000)	1224
θ range for data collection	1.847 to 33.341°.
Index ranges	-31<=h<=31, -12<=k<=12, -24<=l<=24
Reflections collected	37046
Independent reflections	10138 [R(int) = 0.1010]
Completeness to θ = 28.00°	94.7 %
Refinement method	Full-matrix least-squares on F^2
Data / restraints / parameters	10138 / 86 / 497
Goodness-of-fit on F^2	1.076
R_1[a], wR_2[b] [$I>2\sigma(I)$]	0.0629, 0.1620
R_1[a], wR_2[b] (all data)	0.1407, 0.1917
Largest diff. peak and hole	0.877 and -1.491 e.Å^{-3}

[a] $R = \Sigma||F_o| - |F_c||/\Sigma|F_o|$. [b] $wR(F^2) = [\Sigma w(F_o^2 - F_c^2)^2/\Sigma w(F_o^2)^2]^{1/2}$ where $w = 1/[\sigma^2(F_o^2) + (0.0919P)^2 + (0.00)P]$, $P = (F_o^2 + 2F_c^2)/3$.

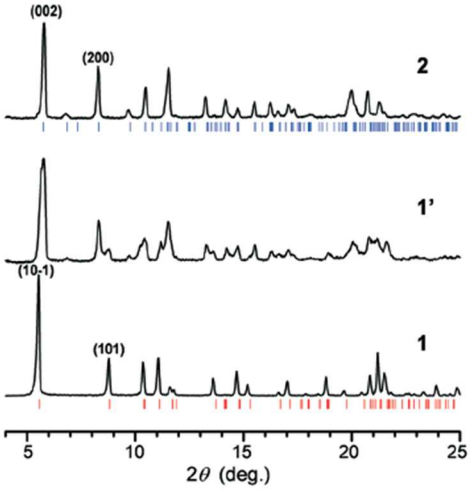

Figure 2. 17. The XRPD patterns of **1**, **1'**, and **2** with simulated (*hkl*) reflections.

The ^{1}H NMR spectra of **1** and **2** also indicate the occurrence of a cycloaddition reaction between the photoactive spy species which produces the rctt-ppcb species. For the NMR measurement, each crystal of **1** and **2** was dissolved in DMSO-d_6 solution with a sulfuric acid-d_2 solution. In sample **1**, the signals for the pyridyl protons at 8.76 ppm and for the olefinic protons at 8.30 ppm (designated as a and b in Figure 2. 18., respectively) show the existence of spy ligands, which are twice that of adipate, in agreement with the crystal structure of 1. In the ^{1}H NMR spectrum of **2**, the appearance of pyridyl peaks at 8.65 ppm and cyclobutane peaks at 5.03 ppm (c and d, respectively) verifies the successful formation of rctt-ppcb. The ratio between the three ligands, spy, rctt-ppcb, and adipate, which is estimated by integration, is also in good agreement with the crystallographic result (spy : rctt-ppcb : adipate = 0.89 : 1.06 : 2.00).

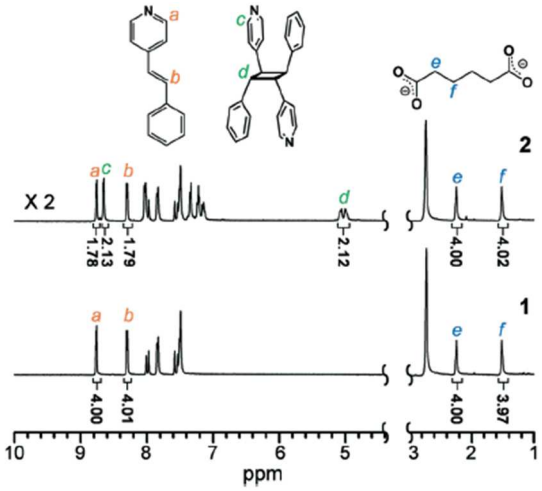

Figure 2. 18. ^{1}H-NMR spectra of **1** and **2.** (the latter trace of **2** is multiplied by 2 for clarity.)

II. 4. Conclusions

In this work, a 2D interdigitated CP, furnished with olefin bond pairs, underwent a solid-state transformation to a 3D CP *via* [2 + 2] photodimerization in a SC–SC manner upon UV irradiation. The SCD investigations revealed that the dynamic atomic rearrangement for both spy and adipate occurred through the photoreactions, including the geometrical change of π–π interactions in spy and the conformational motion of adipate from gauche–anti–gauche to anti–anti–anti. As identified from the structural snapshot of the partially photodimerized compound, the strain accumulation was caused by the coplanar conformational cyclobutane, which has a higher strain energy than the puckered conformation. This reveals that the collective and dynamic movements of the ligands were facilitated owing to the flexible nature of adipate and compensated for the conversion strain. Eventually, the structure was stabilized by these dynamics, which helped the single crystallinity to be retained. The present system provides an interesting design strategy to construct photoreactive CPs or MOFs and monitor the structural transformations in a SC–SC manner.

II. 5. Reference

(1) Kole, G. K.; Vittal, J. J. Solid-state reactivity and structural transformations involving coordination polymers. *Chem. Soc. Rev.,* **2013**, *42*, 1755

(2) Kole, G. K.; Peedikakkal, A. M. P.; Toh, B. M. F.; Vittal, J. J. Solid-State Structural Transformations and Photoreactivity of 1D-Ladder Coordination Polymers of Pbll. *Chem. Eur. J.,* **2013**, *19*, 3962

(3) Medishetty, R.; Husain, A.; Bai. Z.; Runčevski, T.; Dinnebier, R. E.; Naumov, P.; Vittal, J. J. Single Crystals Popping Under UV Light: A Photosalient Effect Triggered by a [2+2] Cycloaddition Reaction. *Angew. Chem., Int. Ed.,* **2014**, *53*, 5907

(4) Yang, C.; Zhu, L.; Kudla, R. A.; Hartman, J. D.; Al-Kaysi, R. O.; Monaco, S.; Schatschneider, B.; Magalhães, A.; Beran, G. J. O.; Bardeen, C. J.; Mueller, L. J. Crystal structure of the meta-stable intermediate in the photomechanical, crystal-to-crystal reaction of 9-tert-butyl anthracene ester. *CrystEngComm,* **2016**, *18*, 7319

(5) Laird, R. C.; Sinnwell, M. A.; Nguyen, N. P.; Swenson, D. C.; Mariappan, S. V. S.; MacGillivray, L. R. Intramolecular [2+2] Photodimerization Achieved in the Solid State *via* Coordination-Driven Self-Assembly. *Org. Lett.,* **2015**, *17*, 3233

(6) Schmidt, G. M. J. PHOTODIMERIZATION IN THE SOLID STATE. *Pure Appl. Chem.,* **1971**, *27*, 647

(7) Bhattacharya, S.; Stojaković, J.; Saha, B. K.; MacGillivray. L. R. A Product of a Templated Solid-State Photodimerization Acts as a Template: Single-Crystal Reactivity in a Single Polymorph of a Cocrystal. *Org. Lett.,* **2013**, *15*, 744

(8) Khan, M.; Enkelmann, V.; Brunklaus, G. Solid-State NMR and X-ray Analysis of Structural Transformations in O-H•••N Heterosynthons Formed by Hydrogen-Bond-Mediated Molecular Recognition. *J. Org. Chem.,* **2009**, *74*, 2261

(9) Caronna, T.; Liantonio, R.; Logothetis, T. A.; Metrangolo, P.; Pilati, T.; Resnati, G. Halogen Bonding and π•••π Stacking Control Reactivity in the Solid State. *J. Am. Chem. Soc.,* **2004**, *126*, 4500

(10) Sarma, B.; Reddy, L. S.; Nangia, A. The Role of π-Stacking in the Composition of Phloroglucinol and Phenazine Cocrystals. *Cryst. Grwoth Des.,* **2008**, *8*, 4546

(11) Sinnwell, M. A.; MacGillivray, L. R. Halogen-Bond-Templated [2+2] Photodimerization in the Solid State: Directed Synthesis and Rare Self-Inclusion of a Halogenated Product. *Angew. Chem.,* **2016**, *128*, 3538

(12) Yan, T.; Sun, L.-Y.; Deng, Y.-X.; Han, Y.-F.; Jin, G.-X. Facile Synthesis of Size-Tunable Functional Polyimidazolium Macrocycles through a Photochemical Closing Strategy. *Chem. Eur. J.,* **2015**, *21*, 17610

(13) Friščić, T.; MacGillivray, L. R. Engineering cocrystal and polymorph architecture *via* pseudoseeding. *Chem. Commun.,* **2009**, *0*, 773

(14) Wang, C.-X.; Gao, Y.; Deng, Y.-X; Lin, Y.-J.; Han, Y.-F.; Jin, G.-X. Photochemical Modification of Carbene-Based Metallacycles: A Facile Route to Polycarbene Complexes and Their Derivatives. *Organometallics.,* **2015**, *34*, 5801

(15) Ando, S.; Fukushima, T.; Yamaguchi, T. Discrete Self-Assembly and Functionality of Guest Molecules in an Organic Framework. *Chem. Mater.,* **2016**, *28*, 5847

(16) Pattabiraman, M.; Natarajan, A.; Kaanumalle, L. S.; Ramamurthy, V. Templating Photodimerization of trans-Cinnamic Acids with Cucurbit[8]uril and γ-Cyclodextrin. *Org. Lett.,* **2005**, *7*, 529

(17) Medishetty, R.; Bai, Z.; Yang, H.; Wong, M. W.; Vittal, J. J. Influence of Fluorine Substitution on the Unusual Solid-State [2+2] Photo-Cycloaddition Reaction between an Olefin and an Aromatic Ring. *Cryst. Growth Des.,* **2015**, *15*, 4055

(18) Kole, G. K.; Tan, G. K.; Vittal, J. J. Anion-Controlled Stereoselective Synthesis of Cyclobutane Derivatives by Solid-State [2+2] Cycloaddition Reaction of the Salts of trans-3-(4-Pyridyl) Acrylic Acid. *Org. Lett.,* **2010**, *12*, 128

(19) Park, I.-H.; Chanthapally, A.; Lee, H.-H.; Quah, H. S.; Lee, S. S.; Vittal, J. J. Solid-state conversion of a MOF to a metal-organo polymeric framework (MOPF) *via* [2+2] cycloaddition reaction. *Chem. Commun.,* **2014**, *50*, 3665

(20) Peedikakkal, A. M. P.; Vittal, J. J. Solid-State Photochemical Behavior of a Triple-Stranded Ladder Coordination Polymer. *Inorg. Chem.,* **2010**, *49*, 10

(21) Park, I.-H.; Mulijanto, C. E.; Lee, H.-H.; Kang, Y.; Lee, E.; Chanthapally, A.; Lee, S. S.; Vittal, J. J. Influence of Interpenetration in Diamondoid Metal-Organic Frameworks on the Photoreactivity and Sensing Properties. *Cryst. Growth Des.,* **2016**, *16*, 2504

(22) Yang, S.-Y.; Deng, X.-L.; Jin, R.-F.; Naumov, P.; Panda, M. K.; Huang, R.-B.; Zheng, L.-S.; Teo, B. K. Crystallographic Snapshots of the Interplay between Reactive Guest and Host Molecules in a Porous Coordination Polymer: Stereochemical Coupling and Feedback Mechanism of Three Photoactive Centers Triggered by UV-Induced Isomerization, Dimerization, and Polymerization Reactions. *J. Am. Chem. Soc.,* **2014**, *136*, 558

(23) Park, I.-H.; Chanthapally, A.; Zhang, Z.; Lee, S. S; Zaworotko, M. J.; Vittal, J. J. Metal-Organic Organopolymeric Hybrid Framework by Reversible [2+2] Cycloaddition Reaction. *Angew. Chem., Int. Ed.,* **2014**, *53*, 414

(24) Foo, M. L.; Matsuda, R.; Hijikata, Y.; Krishna, R.; Sato, H.; Horike, S.; Hori, A.; Duan, J.; Sato, Y.; Kubota, Y.; Takata, M.; Kitagawa, S. An Adsorbate Discriminatory Gate Effect in a Flexible Porous Coordination Polymer for Selective Adsorption of CO_2 over C_2H_2. *J. Am. Chem. Soc.,* **2016**, *138*, 3022

(25) Hazra, A.; Bonakala, S.; Bejagam, K. K.; Balasubramanian, S.; Maji, T. K. Host-Guest [2+2] Cycloaddtion Reaction: Postsynthetic Modulation of CO2 Selectivity and Magnetic Properties in a Bimodal Metal-Organic Framework. *Chem. Eur. J.,* **2016**, *22*, 7792

(26) Claassens, I. E.; Nikolayenko, V. I.; Haynes, D. A.; Barbour, L. J. Solvent-Mediated Synthesis of Cyclobutane Isomers in a Photoactive Cadmium(II) Porous Coordination Polymer. *Angew. Chem., Int. Ed.,* **2018**, *57*, 15563

(27) Kim, T. K.; Lee, K. J.; Choi, M.; Park, N.; Moon, D.; Moon, H. R. Metal-organic frameworks constructed from flexible ditopic ligands: conformational diversity of an aliphatic ligand. *New J. Chem.,* **2013**, *37*, 4130

(28) Kim, T. K; Lee, J. H.; Moon, D.; Moon, H. R. Luminescent Li-Based Metal-Organic Framework Tailored for the Selective Detection of Explosive Nitroaromatic Compounds: Direct Observation of Interaction Sites. *Inorg. Chem.,* **2013**, *52*, 589.

(29) Arvai, A. J.; Nielsen, C. ADSC Quantum-210 ADX Program, Area Detector System Corporation; Poway, CA, USA, 1983

(30) Otwinowski, Z.; Minor, W. Methods in Enzymology, Part A. In Macromolecular Crystallography; Cater Jr., Sweet, C. W.; Eds, R. M.; Academic Press: New York, 1997; Vol.276, pp 307-326

(31) Sheldrick, G. M. SHELXTL-PLUS, Crystal Structure Analysis Package; Bruker Analytical X-Ray; Madison, WI, USA, 1997

(32) Sato, H.; Matsuda, R.; Mir, M. H.; Kitagawa, S. Photochemical cycloaddition on the pore surface of a porous coordination polymer impacts the sorption behavior. Chem, Commun., 2012, 48, 7919

(33) Peedikakkal, A. M. P.; Peh, C. S. Y.; Koh, L. L.; Vittal, J. J. Metal-Organic Frameworks Containing a Tetrapyridylcyclobutane Ligand Derived from Isomerization Reaction. *Inorg. Chem.,* **2010**, *49*, 6775

(34) Paul, A. K.; Karthik, R.; Natarajan, S. Synthesis, Structure, Photochemical [2+2] Cycloaddition, Transformation, and Photocatalytic Studies in a Family of Inorganic-Organic Hybrid Cadmium Thiosulfate Compounds. *Cryst. Growth Des.,* **2011**, *11*, 5741

(35) Medishetty, R.; Tandiana, R.; Koh, L. L.; Vittal, J. J. Assembly of 3D Coordination Polymers from 2D Sheets by [2+2] Cycloaddition Reaction. *Chem. Eur. J.,* **2014**, *20*, 1231

(36) Ou, Y.-C.; Zhi, D.-S.; Liu, W.-T.; Ni, Z.-P.; Tong, M.-L. Single-Crystal-to-Single-Crystal Transformation from 1D Staggered-Sculls Chains to 3D NbO-Type Metal-Organic Framework through [2+2] Photodimerization. *Chem, Eur. J.,* **2012**, *18*, 7357

(37) Brown, W. H.; Iverson, B. L.; Anslyn, E.; Foote, C. S.; Organic Chemistry, Wadsworth Cengage Learning, Belmont, CA, 2014

III. Hetero-structure of Metal-Organic Frameworks : MOF-on-MOF

III. 1. Introduction

Metal-Organic Frameworks (MOFs), also known as Porous Coordination Polymers (PCPs) are intriguing materials with highly crystalline and porosity solid having paid considerable attention recently.[1-3] The assembly of inorganic Secondary Building Units (SBUs) with organic linkers construct a highly ordered crystalline porous structure with distinct features, such as diversified structure[4], large surface area[5], tunable pore size[6] which can be utilized for a desired application. Owing to their properties, MOFs is immersing as promising candidates for a variety of fields such as gas separation[7] and storage[8], drug delivery[9], sensing[10], conduction[11] and catalysis[12]. Moreover, their morphologies also can be observed by Scanning Electron Microscopy (SEM) in nano-sized scale, optical spectroscopy in micro-sized. Structure of MOFs also characterized in molecular level *via* Single Crystal X-Ray Diffraction (SCXRD). Based on those accessible characterization properties, scientists and industry have got interested in MOFs.[13]

The heterostructure of MOFs also has been interested in many researchers. The integration of MOFs with other functional materials such as metal oxides[14], polymer,[15] and nanoparticles[16] are well studied before. Moreover, synthesized the core-shell structure of porous materials emerges as the new class of multifunctional materials.[17] In early research, those core-shell structural-functional porous materials make a better performance than every single component.[18] In this reason, there are already many kinds of MOF@MOF, ZIF (Zeolitic imidazolate framework)@MOF, ZIF@ZIF[19-21] cases are studied, however, they are limited to using the same ligand with different functional group[22,23] or different metal species[24,25]. Otherwise, epitaxial growth of same 2D layer with different pillar ligand so called a block MOF-on-MOF structure.[26] In other words, they have similar lattice parameter with same crystal system. Although lattice mismatched core-shell structure of two different MOFs was studied, they use surfactant or polymers to expedite core-shell structure.[27,28] In these days, few researchers found the un-balanced lattice parameter and crystal system of two MOFs make a core-shell, however, the shell morphology is not clearly shown.[29-31] There was one case of a core-shell structure of different MOFs with maintaining their morphology by Hong-Cai Zhou group.[32] However, the core-shell structure owing to different growth kinetic rate, core MOF is formed first, following shell MOF grow on the core MOF. In other words, not epitaxial growth, but hetero-nucleation.

Herein, our group collaborates with Prof. Jihan Kim at KAIST, who is an authority on the MOF simulation, to make core-shell structure of two different MOFs. According to the algorithm of Kim's group, we get many kinds of possible candidates to make a different core-shell structure of two

different MOFs with different crystal system with similar lattice parameter. Among them, we select UiO-66 (Universitetet i Oslo) as core MOF and MIL-88 (Materials of Institut Lavoisier) as shell MOF. The stable zirconium cluster of UiO-66[33,34] can induce the high temperature during the reaction to form the star shape of core-shell morphology which is evidence of epitaxial growth of shell on the core. As we know, no one has yet managed to synthesize core-shell MOFs based on theoretical predictions. In addition, we utilize the flexible behavior of MIL-88 series, we successfully synthesized UiO-66@MIL-88A-fumarate linker, UiO-66@MIL-88B-terephthalate linker, and UiO-66@MIL-88C-naphthanlate linker core-shell with same star-shaped morphology. Furthermore, as well as shell MOF's ligand length, core MOF's ligand length also controlled to UiO-67-biphenyl dicarboxylate linker. In addition, not only cubic/hexagonal pairs but also cubic/cubic pair which is UiO-67@HKUST-1 also discussed with the different morphology result. Their crystallinity and formation of MOFs are characterized by X-Ray Powder Diffraction patterns (XRPD). The morphology is observed by SEM and Transmission Electron Microscopy (TEM) and the metal composition of core and shell is observed by Scanning & Transmission Electron Microscopy–Energy Dispersive x-ray Spectroscopy (STEM-EDS).

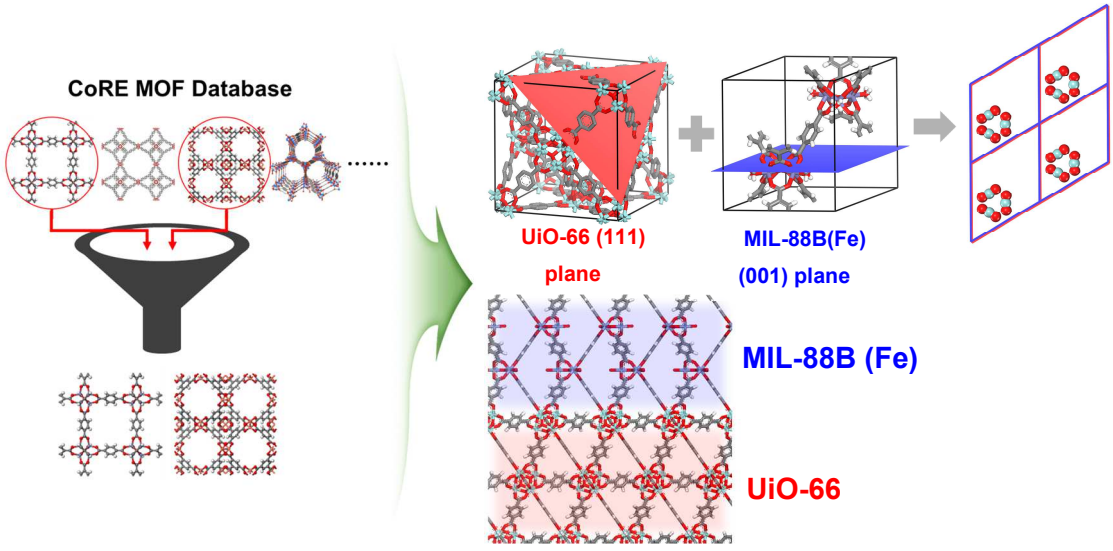

III. 2. Experiment Section

Materials and Methods.

All chemicals and solvents were of reagent grade and used without further purification. X-ray powder diffraction (XRPD) data were recorded on a Bruker D2 phaser diffractometer at 30 kV and 10 mA for Cu Kα (λ = 1.541 Å), with a step size of 0.02º in 2θ. Transmission electron microscopy (TEM), Scanning transmission electron microscopy (STEM), Energy-dispersive x-ray spectroscopy (EDS) images were taken using a FEI Tecnai G2 F20 X-Twin TEM, JEOL JEM-2100F microscope. Scanning electron microscopy (SEM) images were taken using a Hitach High-Technologies Cold FE-SEM operating at 10 kV.

Synthesis of *S*-UiO-66[35]

$ZrCl_4$ (0.0530 g, 0.228 mmol) and terephthalic acid (H_2BDC) (0.0379 g, 0.227 mmol) in dimethylformamide (DMF) (26 mL) were sealed and placed in 120 ℃ oven and kept for 24 hours. The white powder was collected by centrifugation, washed 3 times with DMF and dried at vacuum oven at room temperature overnight.

Synthesis of *L*-UiO-66[36]

H_2BDC (0.100 g, 0.602 mmol) and triethylamine (TEA) (0.01 mL) were dissolved in 140 mL of DMF in 250 mL round-bottom flask and stirred (600 rpm) for 10 minutes before the addition of acetic acid (20.6 mL). The flask was placed in an oil bath and heated to 120 ℃. After the temperature of the oil bath reached 120 °C, 10 mL of DMF solution containing $ZrCl_4$ (0.140 g, 0.601 mmol) was added. After 6 hours, the white powder was collected by centrifugation, washed 3 times with DMF and dried at vacuum oven at room temperature overnight.

Synthesis of UiO-67[37]

$ZrCl_4$ (0.0186 g, 0.0798 mmol) and acetic acid (1.38 mL) were dissolved in DMF (5 mL). 4,4'-biphenyldicarboxylic acid (H_2BPDC) (0.0193 g, 0.0797 mmol) and TEA(30 μL) were dissolved in DMF (5 mL). Each solution was sonicated for 10 min and combined in 20 mL *via*l. The combined solution was further sonicated for 10 min and placed at 85 ℃ oven. After 8 hours, the white powder was collected by centrifugation and washed 3 times with DMF and dried at vacuum oven at room temperature overnight.

Synthesis of MIL-88A[38]

Fumaric acid (0.0487 g, 0.422 mmol) and $FeCl_3 \cdot 6H_2O$ (0.114 g, 0.422 mmol) were dissolved in 10 mL of distilled water. The mixture was placed in a Teflon vessel within the autoclave and heated 85 ℃ for 6 hours. The orange powder was collected by centrifugation and washed 3 times with distilled water.

Synthesis of MIL-88B[39]

H_2BDC (0.266 g, 1.60 mmol) and $FeCl_3 \cdot 6H_2O$ (0.432 g, 1.60 mmol) were dissolved in DMF (8 mL) with 2 M NaOH (0.64 mL). The mixture was placed in Teflon vessel within the autoclave, and heated 100 ℃ for 8 hours with a heating ramp of 3 ℃/min. The orange powder was collected by centrifugation and washed 3 times with DMF.

Synthesis of MIL-88C[40]

2,6-naphthalene dicarboxylic acid (H_2NDC) (2.08 g, 9.62 mmol) and $FeCl_3 \cdot 6H_2O$ (2.56 g, 9.47 mmol) were dissolved in DMF (100 mL). The mixture was placed in a 250 mL round-bottom flask and heated at 130 ℃ for 18 hours with stirring (300rpm). The orange powder was collected by centrifugation and washed 3 times with DMF.

Synthesis of UiO-66@MIL-88A core-shell.

20 mg of UiO-66 were added to a 5 mL aqueous solution of fumaric acid (0.0487 g, 0.422 mmol) and sonicated for 90 minutes. 5 mL of distilled water solution containing $FeCl_3 \cdot 6H_2O$ (0.114 g, 0.422 mmol) was added to the solution. The mixture was transferred to Teflon vessel within the autoclave and heated at 85 ^oC. After 6 hours, the orange powder was collected by centrifugation and washed 3 times with distilled water.

Synthesis of UiO-66@MIL-88B core-shell.

20 mg of UiO-66 were added to a 3 mL DMF solution containing H_2BDC (0.0553g, 0.333 mmol) and sonicated for 90 minutes. $FeCl_3 \cdot 6H_2O$ (0.0900 g, 0.333 mmol) in 2 mL of DMF solution was fully dissolved by adding 0.4 mL of NaOH solution (0.67 M) and added to the solution. The mixture was transferred to Teflon vessel within the autoclave and heated to 100 °C with heating ramp of 3°C/min. After 8 hours, the orange powder was collected by centrifugation and washed 3 times with distilled water.

Synthesis of UiO-66@MIL-88C core-shell.

20 mg of UiO-66 were added to a 5 mL of DMF solution containing H_2NDC (0.100 g, 0.409 mmol) and sonicated for 90 minutes. 5 mL of DMF solution containing $FeCl_3 \cdot 6H_2O$ (0.128 g, 0.473 mmol) was added to the solution. The mixture was transferred to 100 mL round-bottom flask and heated to 130 °C with stirring (300rpm). After 18 hours, the orange powder was collected by centrifugation and washed 3 times with DMF.

Synthesis of UiO-67@MIL-88C core-shell.

20 mg of UiO-67 were added to a 5 mL of DMF solution containing H_2NDC (0.100 g, 0.409 mmol) and sonicated for 90 minutes. 5 mL of DMF solution containing $FeCl_3 \cdot 6H_2O$ (0.128 g, 0.473 mmol) was added to the solution. The mixture was transferred to 250 mL round-bottom flask and heated to 130 °C with stirring (300rpm). After 18 hours, the orange powder was collected by centrifugation and washed 3 times with DMF.

Synthesis of UiO-67@HKUST-1[41]

20 mg of UiO-67 were added to a MeOH (25 mL) solution with benzene-1,3,5-tricarboxylic acid (H_3BTC) (0.0800 g, 0.381 mmol) and sonicated for 90 minutes. 25 mL of methanol solution containing $Cu(NO_3)_2 \cdot 2.5H_2O$ (0.910 g, 3.91 mmol) was added to the solution. The mixture was transferred to a 100 mL *via*l, sonicated for 10 min, and placed in room temperature for 2 hours. The blue powder was collected by centrifugation and washed 3 times with methanol.

III. 3. Result and Discussion

Collaborate with Professor Jihan Kim's group, hetero core-shell structure of MOFs was considered in our laboratory. However, over 6,000 crystal structures have been reported to CSD (Cambridge Structural Database) and 29, 700 SCI papers have been published already. Therefore, they should pick candidates out for simple calculation.[42] Consequently, they use CoRE MOF database and selected the simplest case candidates, hexagonal and cubic. Among them, UiO-66 and MIL-88B are selected owing to cell parameter difference (14.6374 Å and 14.4162 Å for (111) plane of UiO-66 and (001) plane of MIL-88B, respective; 1.51 % of mismatch), commercially available precursors, and simple synthetic process. (Figure 3. 1.)

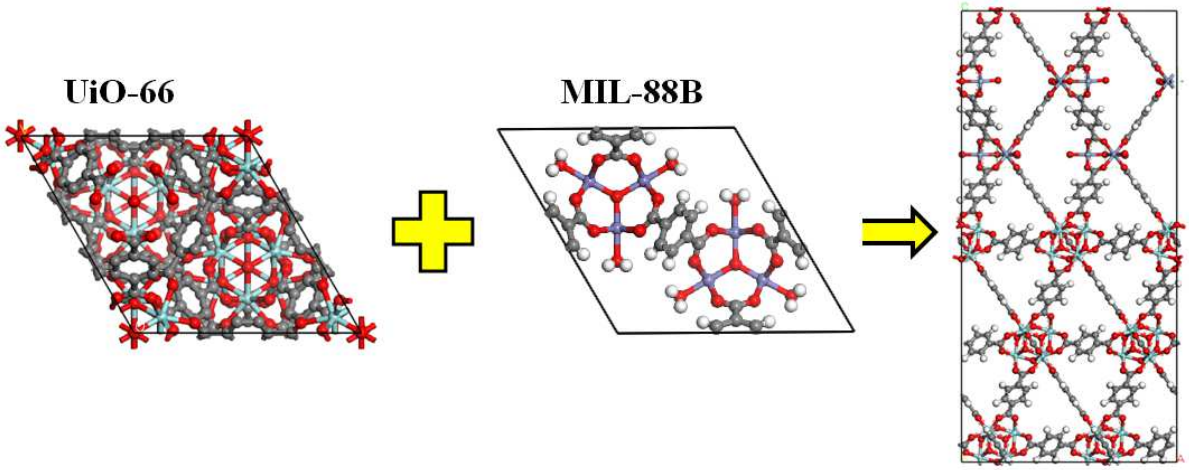

Figure 3. 1. Schematic design of simulation result of UiO-66 and MIL-88B and cell parameter difference.

Both two MOFs have same terephthalate ligand, however, the connectivity of ligand and metal is different, and crystal system also different. UiO-66, which is a cubic crystal system (Fm-3m space group with a = 20.7004(2) Å), has $Zr_6O_4(OH)_4$ core in which the triangular faces of the Zr_6-octahedron are alternatively capped by μ_3-O and μ_3-OH groups. Every edge of the polyhedron is connected by carboxylates of terephthalate forming 12-coordinated zirconium based $Zr_6O_4(OH)_4(CO_2)_{12}$ cluster with exceptional stability.[35] MIL-88B, which is a hexagonal crystal system ($P6_3/mmc$ space group with a=b=14.416 Å, c=17.304 Å) has trimers of iron(III) octahedra cluster that shares a μ_3-O and each iron connected by carboxylates of terephthalate.[39] Because of high stability, UiO-66 select as core MOF and MIL-88B act as shell MOF.

UiO-66 synthesized by solvothermal reaction with zirconium chloride and terephthalic acid in Teflon-lined autoclave at 100 ℃ for 8 hours. However, morphology of UiO-66 not clearly appeared when synthesized without modulator (Figure 3. 2. (a)), which makes hard to observed product of a core-shell reaction. Therefore, by using TEA and acetic acid for synthesis defined variation of particle sizes and shapes around 700~1000 nm octahedral as exposed to (111) plane in eight facets morphology of UiO-66 shown as SEM images. (Figure 3. 2. (b)) The crystallinity also confirmed by XRPD pattern. (Figure 3. 2. (c))

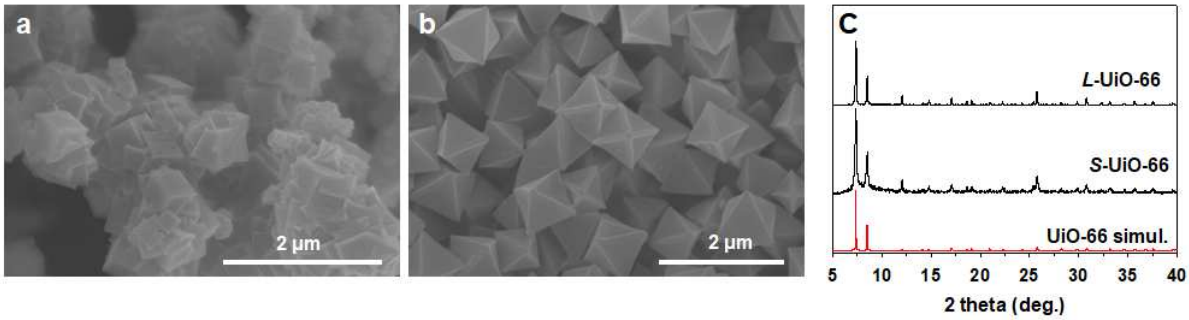

Figure 3. 2. (a) SEM image of UiO-66 without modulator (S means small) (b) SEM image of UiO-66 with modulator (L means large) From here, *L*-UiO-66 denoted as UiO-66 (c) XRPD patterns of UiO-66

MIL-88B also synthesized by solvothermal reaction with Teflon-lined autoclave. Iron (III) chloride, terephthalic acid, and sodium hydroxide solution at 100 ºC for 8 hours gave rise orange powder which observed as hexagonal rod shape morphology by SEM images. (Figure 3. 3. (a)) Also, XRPD pattern is well matched with the simulated pattern. (Figure 3. 3. (b))

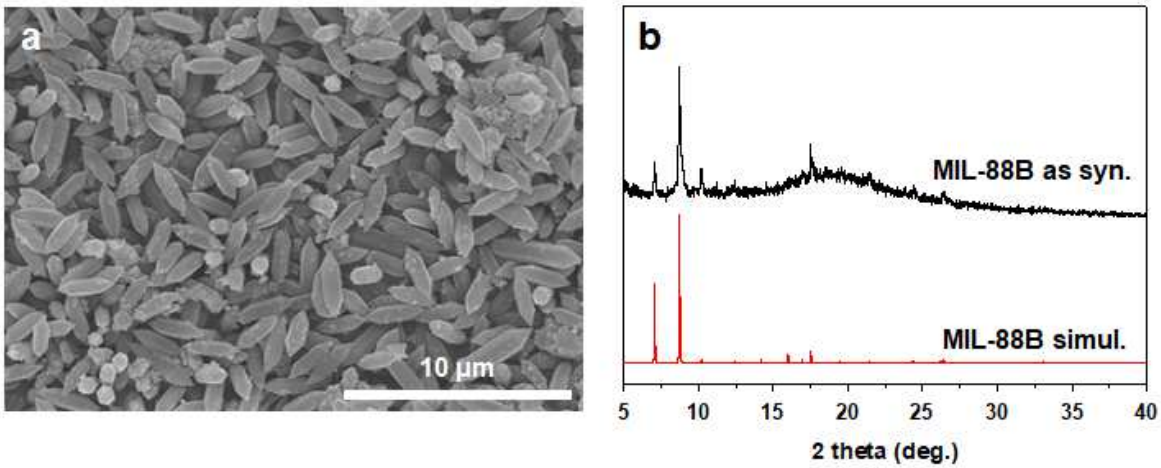

Figure 3. 3. (a) SEM images of MIL-88B (b) XRPD patterns of MIL-88B

To synthesized core-shell structure of UiO-66@MIL-88B, 20 mg of UiO-66 was sonicated with the terephthalic acid solution to well dispersing the UiO-66 in solution to avoid aggregate each other which interrupt the interaction with precursors of MIL-88B. The {001} plane of MIL-88B start to grow on exposed {111} plane of UiO-66 produced star-shaped morphology core-shell structure which is strong evidence of epitaxial growth. All characteristic peaks of MIL-88B and UiO-66 were shown in XRPD, demonstrating UiO-66 and MIL-88B coexistence. (Figure 3. 4. (a)) Moreover, homogeneous core-shell morphology with very small amount of MIL-88B was shown in the SEM image also indicate a successful synthesis of core-shell. (Figure 3. 4. (c)) In addition, STEM-EDS images display a well distribution of zirconium atoms in the core region, indicate UiO-66, whereas, iron atoms were found entire particle but mainly on the shell, which is MIL-88B. (Figure 3. 4. (d)) We also investigated the growth behaviors of MIL-88B on the UiO-66 substrate according to reaction time. After an hour, small islands MIL-88B grow on each (111) plane of UiO-66. As times go, each small MIL-88B combined into the larger triangular pyramidal structure after 4 hours. Interestingly, the eight triangular pyramidal pieces on the eight triangular sides of the octahedron did not coalesce into a larger single crystal, contrast with other MOF@MOF core-shell structure. This phenomenon to the fact that the two components have different crystal systems and the crystal growth directions of the multiple shell MOFs from the different {111} surfaces of the core MOF are not crystallo-graphically compatible to each other (Figure 3. 4. (e)) This phenomenon provides evidence that the UiO-66 substrate plays a primary role in directing the growth of MIL-88B crystals

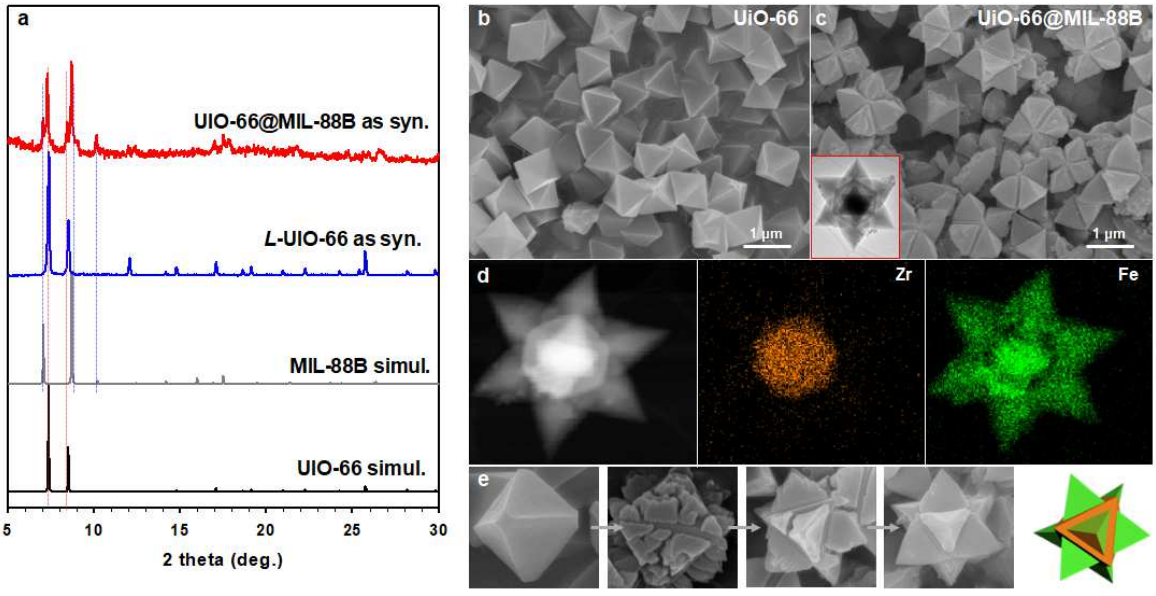

Figure 3. 4. (a) XRPD patterns of Core-shell MOF. (b) SEM image of UiO-66. (c) SEM and inset TEM images of UiO-66@MIL-88B (d) STEM-EDS images with zirconium and iron mapping. (f) Core-shell structure reaction process. From left to right, 0 h, 1 h, 2 h, 4 h.

Interestingly, at early moment, excess MIL-88B is rarely appeared. However, after 12 hours, excess MIL-88B is observed. This phenomenon is already known by classic nucleation theory that hetero-nucleation is favor than homo-nucleation. Further reaction than 12 hours, small particles are appeared which seems decreased purity and crystallinity of UiO-66@MIL-88B. Star-shaped morphologies were collapse and small particles appeared in SEM image. In 48 hours, almost every triangular pyramidal MIL-88B is disappeared. (Figure 3. 5.) In addition, any other peak doesn't appear except UiO-66 at XRPD patterns, demonstrated the degradation of MIL-88B. (Figure 3. 6)

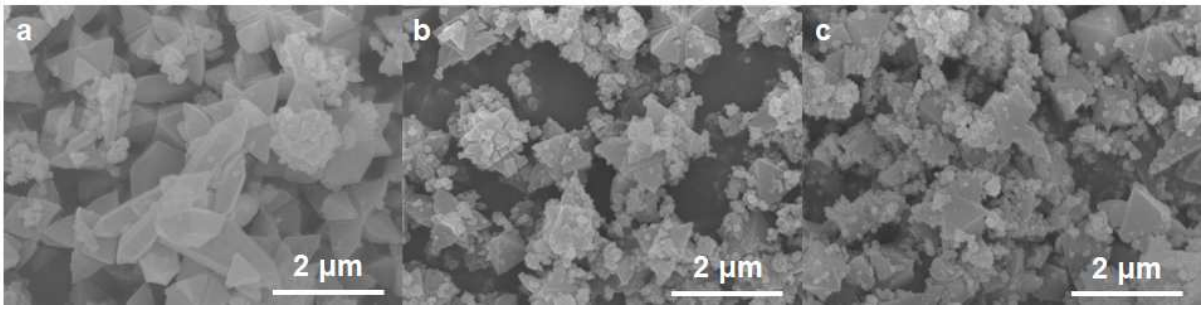

Figure 3. 5. SEM images of UiO-66@MIL-88B at (a) 12 h (b) 24 h (c) 48 h

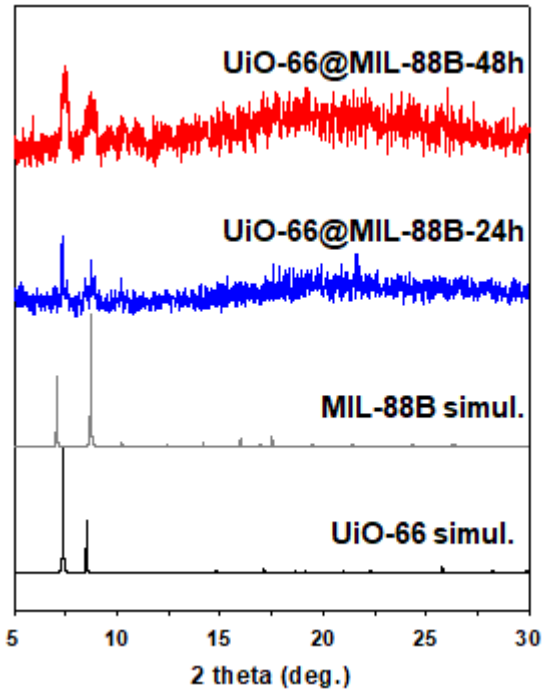

Figure 3. 6. XRPD patterns of UiO-66@MIL-88B at different reaction time.

Moreover, MIL-88B already known for its flexibility in the previous study, so, we conduct a flexibility control experiment by solvent exchange or activation by heating under vacuum. First, as synthesized MIL-88B clearly show its flexible behavior in XRPD patterns. As already known, when the cell is dried, the c-axis elongated, which causes XRPD peak stands for (002) plane shifts to lower angles and a, b-axis become compressed, which causes XRPD peak stands for (100) and (101) planes shift to higher angles. Those peak shifts are clearly observed in XRPD and well matched with simulated patterns. (Figure 3. 7. (a)) In core-shell case, the characteristic peak of MIL-88B is shown in as-syn XRPD pattern, and when exchanging the solvent with H_2O three times following acetone three times, UiO-66@MIL-88B show characteristic peak of activated MIL-88B and UiO-66 which are well matched with a simulated pattern. (Figure 3. 7. (b)) However, in SEM images, UiO-66 core and MIL-88B shell are separated with maintaining both morphologies. The result is reasonable if considering the extreme level of structural transformability of the MIL-88B series upon the application of external stimuli. An abrupt and sudden change of the unit cell in MIL-88B(Fe) connected to rigid UiO-66 structure would cause strong stress on the boundary between the two materials and eventually separate them. It is another evidence of epitaxial growth because the connection between (111) plane of UiO-66 and (001) plane of MIL-88B couldn't withstand the strain of cell expansion causes separate of both MOFs. (Figure 3. 8.)

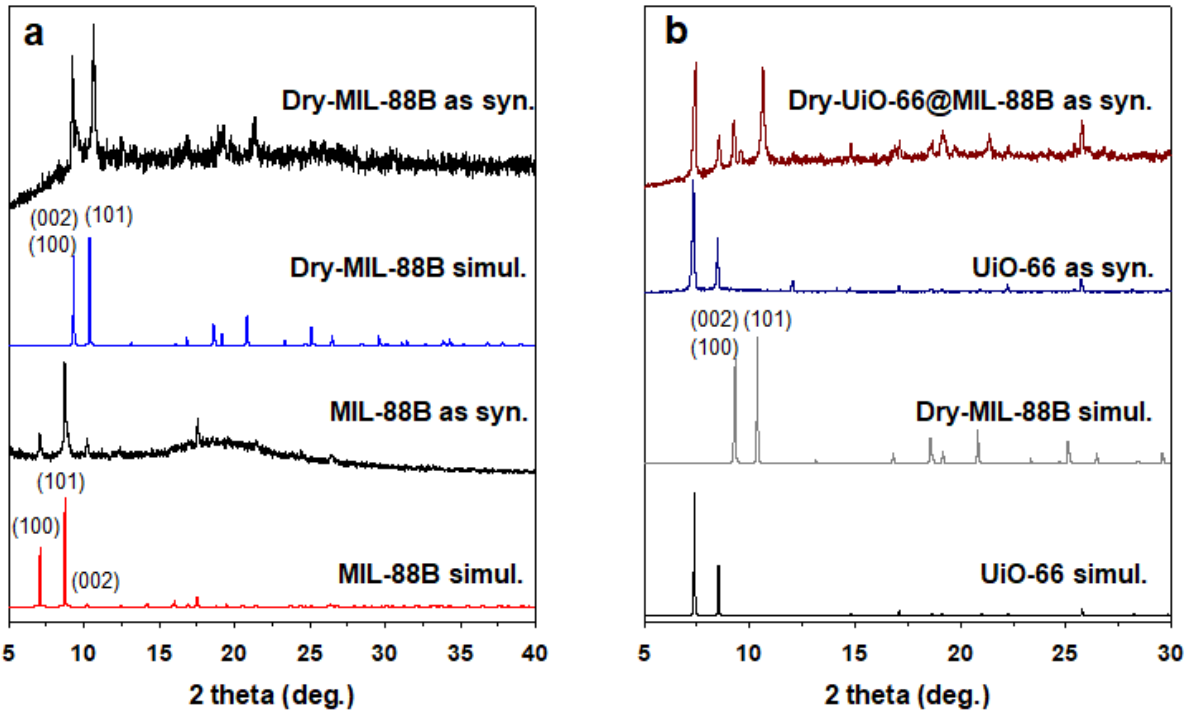

Figure 3. 7. XRPD patterns of (a) MIL-88B and dry form of MIL-88B. (b) Dry form of UiO-66@MIL-88B.

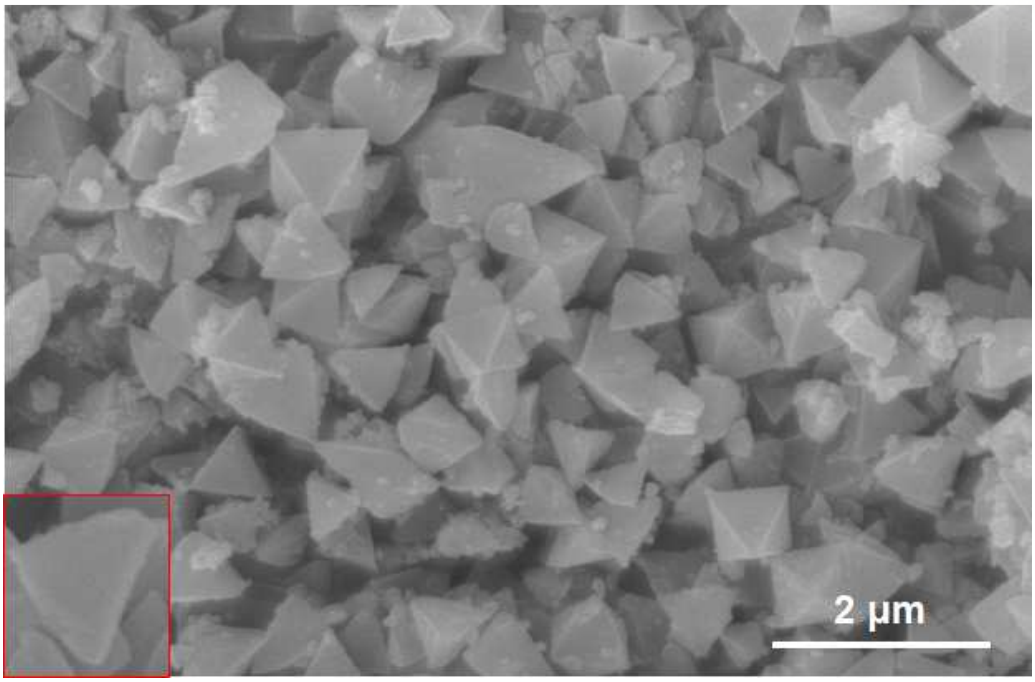

Figure 3. 8. SEM images of dry UiO-66@MIL-88B red box show separate MIL-88B. (Inset box is separate MIL-88B)

Finally, we expanded several core-shell pairs which have same $Zr_6O_4(OH)_4(CO_2)_{12}$ cluster core with a different ligand, biphenyl-4,4'-dicarboxylic acid (BPDC), UiO-67 and trimers of iron (III) octahedra cluster shell with different ligands, fumaric acid and NDC, which indicate MIL-88A and MIL-88C. According to the previous work conducted by Serre et al[42], isoreticular analogues, MIL-88A to MIL-88C has a large degree of flexibility upon external stimuli and in different environment. Therefore, the cell parameter range of MIL-88 series is summarized in Figure 3. 9.

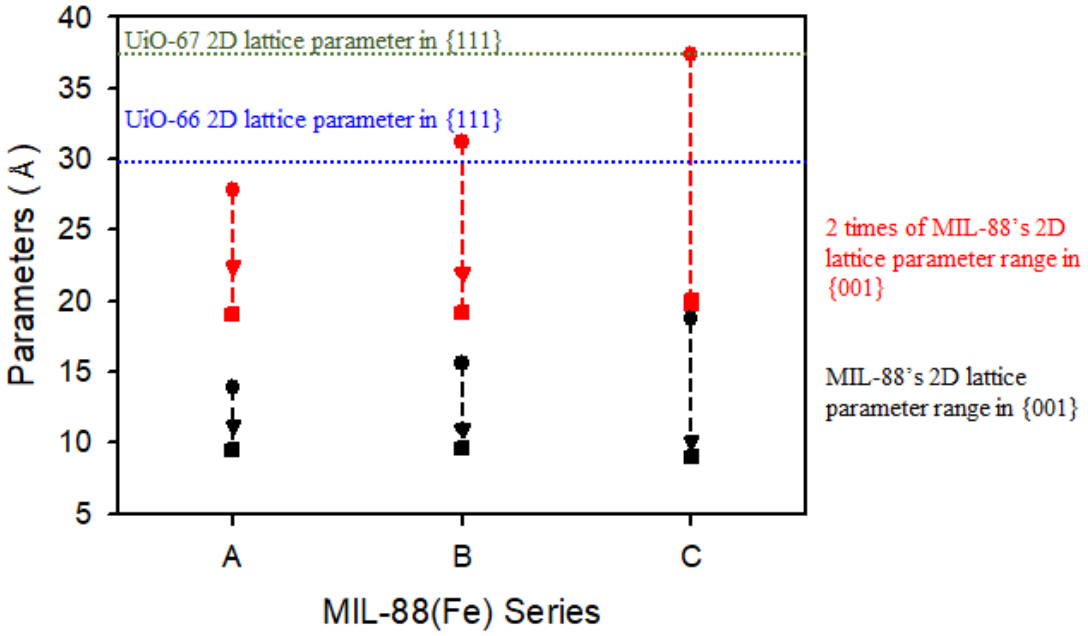

Figure 3. 9. 2D Lattice parameters of MIL-88 series. Black symbols are flexible ranges of 2D lattice parameter in {001} surface of MIL-88 series and red symbols are 2 times of flexible ranges of 2D lattice parameter in {001} surface of MIL-88 series. Blue dotted line is 2D lattice parameter of UiO-66,67 in {111} surface.

As shown in Figure 3. 9, UiO-66@MIL-88A, UiO-66@MIL-88B, UiO-67@MIL-88C almost match each other in terms of shell MOFs' flexible range. Obviously, those pairs successfully derive the core-shell structures. Although MIL-88 series doesn't have desired cell parameter at the synthetic condition, the lattice parameters of {001} of those compounds undergo extensive changes, being transferred from the dry phase to the open, which approximate that of UiO-66,67 in {111} surface. As such, the hinge effect of flexible MOFs can be exploited to structurally compensate for the lattice mismatches at the interface between the two connected MOFs. However, owing to the large cell difference between two MOFs, UiO-67@MIL-88A, UiO-67@MIL-88B pairs doesn't form the core-shell structure.

Then, we measured the XRPD patterns for confirmed the formation of the shell. (Figure 3. 9.) In all case, the characteristic peak of shell MOFs is shown in XRPD patterns demonstrating successful synthesized of shell MOFs. Moreover, in SEM images, star-shaped morphology of pairs is shown, which is the same result as UiO-66@MIL-88B case. (Figure 3. 10.)

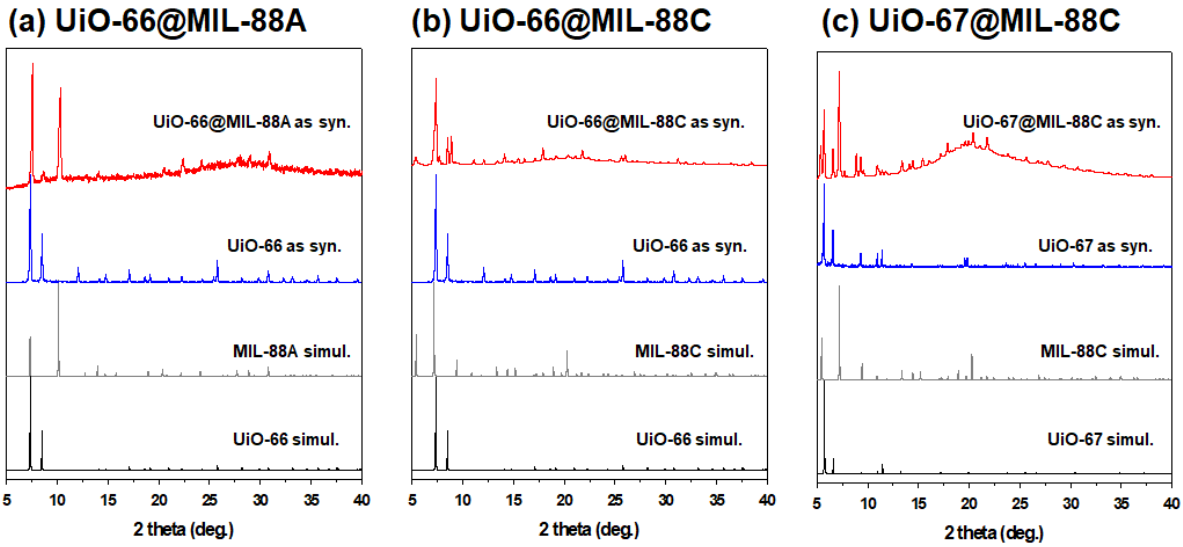

Figure 3. 10. XRPD of (a) UiO-66@MIL-88A (b) UiO-66@MIL-88C (c) UiO-67@MIL-88C core-shell pairs.

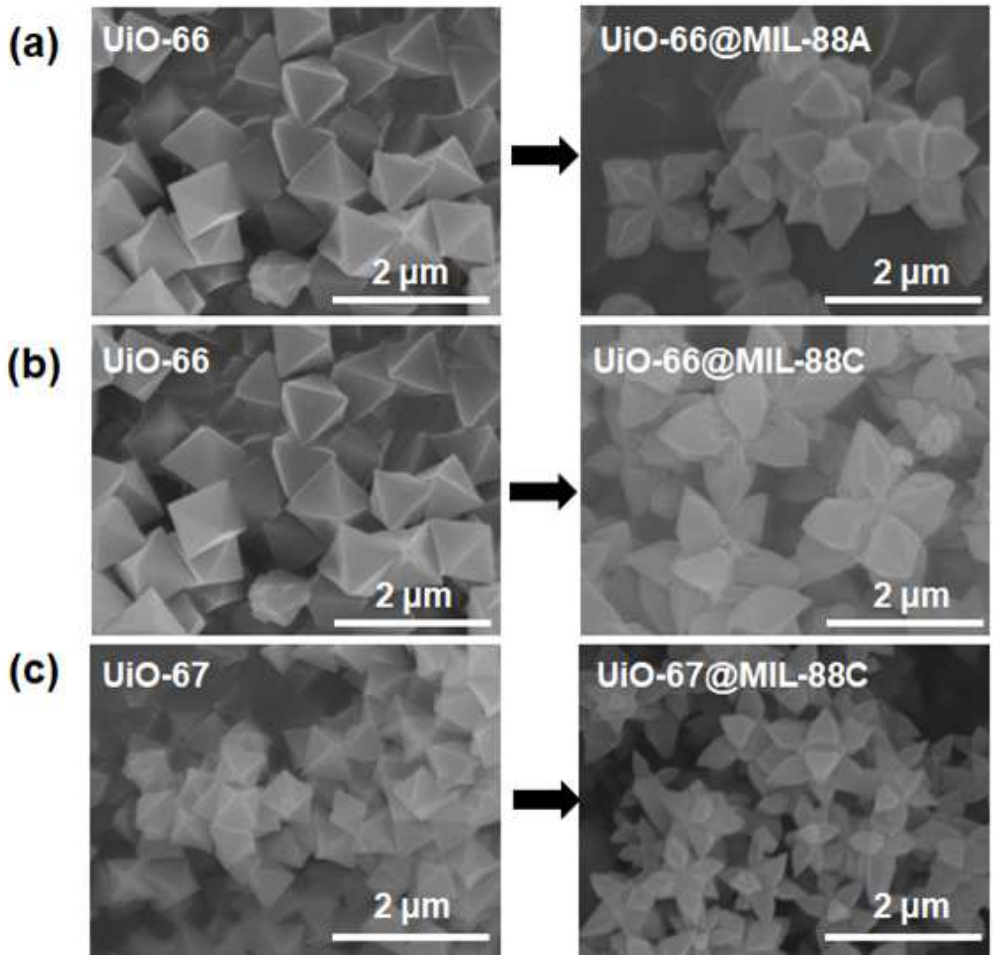

Figure 3. 11. SEM images of UiO-66, 67 and (a) UiO-66@MIL-88B (b) UiO-66@MIL-88C (c) UiO-67@MIL-88C.

In order to expand our experiment for further generalization, we conducted cubic/cubic core-shell case. In this case, (111) plane of core MOF and (111) plane of shell MOF were calculated. As a result, UiO-67 (Fm-3m space group with a = 26.768(5) Å) and HKUST-1 (Fm-3m space group with 26.3867(2) Å) are selected as candidates for core-shell pair. Synthesis of HKUST-1 is observed by XRPD pattern with SEM images. (Figure 3. 11.) The smooth octahedral {111} surface of UiO-67 changed to the rough surface which is evidence of the growth of HKUST-1. Also, In STEM-EDS images, we can clearly observe the zirconium atoms fill in the core and cupper atoms mainly dispersed in shell. (Figure 3. 12.) Compared with star-shaped UiO-66@MIL-88B, HKUST-1 perfectly cover the whole UiO-67. It is also explained by crystal growth direction as above. In this case, the crystal growth direction of shell MOF is similar to core MOF consequently derived whole covered core-shell morphology of core-shell MOF.

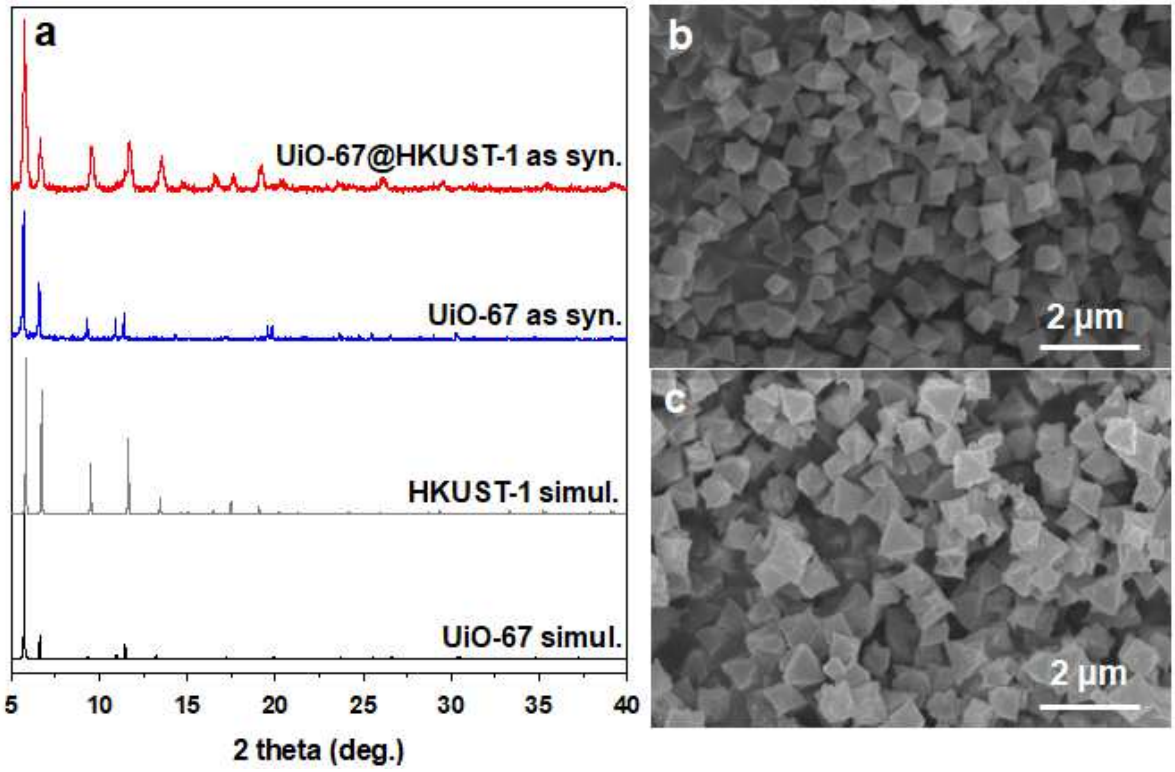

Figure 3. 12. (a) XRPD patterns of UiO-67@HKUST-1 (b) SEM images of UiO-67 (c) UiO-67@HKUST-1

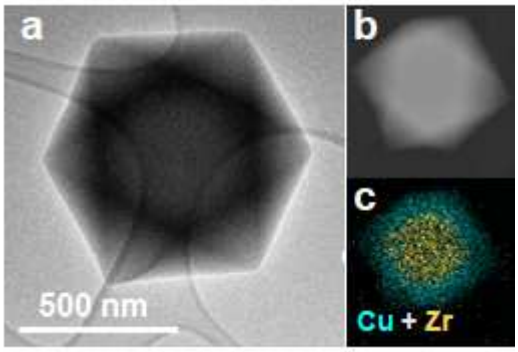

Figure 3. 13. UiO-67@HKUST-1 (a) TEM image (b) STEM image (c) EDS mapping Colour scheme : Zr : orange; Cu : turquoise

III. 4. Conclusions

In this work, based on simulation by Prof. Jihan Kim group at KAIST, we searched out several possible candidates, which could be core-shell structure, consequently, successfully synthesized the core-shell structure of UiO-66 and MIL-88B. The stable UiO-66 act as core MOF, and flexible MIL-88B act as shell MOF. (001) the plane of MIL-88B grows on the 8 triangular faces of (111) plane of UiO-66 to form star-shaped morphology owing to cell mismatch between the grown shell and growing shell. In contrast with previous work, our work used two different MOFs with different crystal structures. Although both MOFs use same terephthalate ligand, however, the coordination state is different, in case of UiO-66 Zr_6-cluster and MIL-88B has $Fe_3(\mu_3\text{-O})$ clusters. In addition, the morphology of shell MOF also maintains after reaction which is evidence of epitaxial growth. Moreover, we utilize the flexibility of MIL-88 series, successfully synthesized UiO-66@MIL-88A, UiO-66@MIL-88C, UiO-67@MIL-88C. Furthermore, we expand our experiment with cubic/cubic core-shell pair for further generalization, in case of UiO-67@HKUST-1. This study is the first case synthesize core-shell MOFs based on theoretical predictions. We hope this work make a new paradigm of the heterostructure of MOF, especially, MOF@MOF core-shell structure.

III. 5. Reference

(1) Moulton, B.; Zaworotko, M. J. From Molecules to Crystal Engineering: Supramolecular Isomerism and Polymorphism in Network Solids. *Chem. Rev.,* **2001**, *101,* 1629

(2) O'Keeffe, M.; Peskov, M. A.; Ramsden, S. J.; Yaghi, O. M.; The Reticular Chemistry Structure Resource (RCSR) Database of, and Symbols for, Crystal Nets. *Acc. Chem. Res.,* **2008**, *41,* 1782

(3) Furukawa, S.; Reboul, J.; Diring, S.; Sumida, K.; Kitagawa, S. Structuring of metal-organic frameworks at the mesoscopic/macroscopic scale. *Chem. Soc. Rev.,* **2014**, *43,* 5700

(4) Lu, W.; Wei, Z.; Gu, Z.-Y.; Liu, T.-F.; Park, J.; Park, J.; Tian, J.; Zhang, M.; Zhang, Q.; Gentle III, T.; Bosch, M.; Zhou, H.-C. Tuning the structure and function of metal-organic frameworks *via* linker design. *Chem. Soc. Rev.,* **2014**, *43,* 5561

(5) Furukawa, H.; Ko, N.; Go, Y. B.; Aratani, N.; Choi, S. B.; Choi, E.; Yazaydin, A. Ö.; Snurr, R. Q.; O'Keeffe, M.; Kim, J.; Yaghi, O. M. Ultrahigh Porosity in Metal-Organic Frameworks. *Science,* **2010**, *329,* 424

(6) Du, L.; Lu, Z.; Zheng, K.; Wang, J.; Zheng, X.; Pan, Y.; You, X.; Bai, J. Fine-Tuning Pore Size by Shifting Coordination Sites of Ligands and Surface Polarization of Metal-Organic Frameworks To Sharply Enhance the Selectivity for CO_2. *J. Am. Chem. Soc.,* **2013**, *135,* 562

(7) Li, J.-R.; Sculley, J.; Zhou, H.-C. Metal-Organic Frameworks for Separations. *Chem. Rev.,* **2012**, *112,* 869

(8) Suh, M. P.; Park, H. J.; Prasad, T. K.; Lim, D.-W.; Hydrogen Storage in Metal-Organic Frameworks. *Chem. Rev.,* **2012**, *112,* 782

(9) Horcajada, P.; Gref, R.; Baati, T.; Allan, P. K.; Maurin, G.; Couvreur, P.; Férey, G.; Morris, R. E.; Serre, C. Metal-Organic Frameworks in Biomedicine. *Chem. Rev.,* **2012**, *112,* 1232

(10) Kreno, L. E.; Leong, K.; Farha, O. K.; Allendorf, M.; Duyne, R. P. V.; Hupp, J. T. Metal-Organic Framework Materials as Chemical Sensors. *Chem. Rev.,* **2012**, 1105

(11) Sun, L.; Campbell, M. G.; Dincă, M. Electrically Conductive Porous Metal-Organic Frameworks. *Angew. Chem. Int. Ed.,* **2016**, *55,* 3566

(12) Huang, Y.-B.; Liang, J.; Wang, X.-S.; Cao, R. Multifunctional metal-organic framework catalysts: synergistic catalysis and tandem reactions. *Chem, Soc, Rev.,* **2017**, *46*, 126

(13) Czaja, A. U.; Trukhan, N.; Müller, U. Industrial applications of metal-organic frameworks. *Chem. Soc. Rev.,* **2009**, *38*, 1284

(14) Yu, B.; Wang, F.; Dong, W.; Hou, J.; Lu, P.; Gong, J. Self-template synthesis of core-shell ZnO@ZIF-8 nanospheres and the photocatalysis under UV irradiation. *Mat. Lett.,* **2015**, *156,* 50

(15) Lee, H. J.; Cho, W.; Oh, M. Advanced fabrication of metal-organic frameworks: template-directed formation of polystyrene@ZIF-8 core-shell and hollow ZIF-8 microspheres. *Chem. Commun.,* **2012**, *48,* 221

(16) Liu, Y.; Tang, Z. Multifunctional Nanoparticle@MOF Core-Shell Nanostructures. *Adv. Mater.,* **2013**, *25*, 5819

(17) Koh, K.; Wong-Foy, A. G.; Matzger, A. J. MOF@MOF: microporous core-shell architectures. *Chem. Commun.,* **2009**, *0*, 6162.

(18) Li, T.; Sullivan, J. E.; Rosi, N. L. Design and Preparation of a Core-Shell Metal-Organic Framework for Selective CO_2 Capture. *J. Am. Chem. Soc.,* **2013**, *135*, 9984

(19) Ji, H.; Lee, S.; Park, J.; Kim, T.; Choi, S.; Oh, M.; Improvement in Crystallinity and Porosity of Poorly Crystalline Metal-Organic Frameworks (MOFs) through Their Induced Growth on a Well-Crystalline MOF Template. *Inorg. Chem.,* **2018**, *57*, 9048

(20) Song, Z.; Qiu, F.; Zaia, E. W.; Wang, Z.; Kunz, M.; Guo, J.; Brady, M.; Mi, B.; Urban, J. J. Dual-Channel, Molecular-Sieving Core/Shell ZIF@MOF Architectures as Engineered Fillers in Hybrid Membranes for Highly Selective CO_2 Separation. *Nano Lett.,* **2017**, *17*, 6752

(21) Panchariya, D. K.; Rai, R. K.; Kumar, E. A.; Singh, S. K. Core-Shell Zeolitic Imidazolate Frameworks for Enhanced Hydrogen Storage. *ACS Omega.,* **2018**, *3*, 167

(22) Hirai, K.; Furukawa, S.; Kondo, M.; Uehara, H.; Sakata, O.; Kitagawa, S. Sequential Functionalization of Porous Coordination Polymer Crystals. *Angew. Chem. Int. Ed.,* **2011**, *50,* 8057

(23) Boissonnault, J. A.; Wong-Foy, A. G.; Matzger, A. J. Core-Shell Structures Arise Naturally During Ligand Exchange in Metal-Organic Frameworks. *J. Am. Chem. Soc.,* **2017**, *139*, 14841

(24) Shekhah, O.; Hirai, K.; Wang, H.; Uehara, H.; Kondo, M.; Diring, S.; Zacher, D.; Fischer, R. A.; Sakata, O.; Kitagawa, S.; Furukawa, S.; Wőll, C. MOF-on-MOF heteroepitaxy: perfectly oriented $[Zn_2(ndc)_2(dabco)]_n$ grown on $[Cu_2(ndc)_2(dabco)]_n$ thin films. *Dalton Trans.,* **2011**, *40*, 4954

(25) Luo, T.-Y.; Liu, C.; Gan, X. Y.; Muldoon, P. F.; Diemler, N. A.; Millstone, J. E.; Rosi, N. L. Multivariate Stratified Metal-Organic Frameworks: Diversification Using Domain Building Blocks. *J. Am. Chem. Soc.,* **2019**, *141*, 2161

(26) Furukawa, S.; Hirai, K.; Takashima, Y.; Nakagawa, K.; Kondo, M.; Tsuruoka, T.; Sakata, O.; Kitagawa, S. A block PCP crystal: anisotropic hybridization of porous coordination polymers by face-selective epitaxial growth. *Chem. Commun.,* **2009**, *0*, 5097

(27) Gu, Y.; Wu, Y.-n.; Li, L.; Chen, W.; Li, F.; Kitagawa, S. Controllable Modular Growth of Hierarchical MOF-on-MOF Architectures. *Angew. Chem. Int. Ed.,* **2017**, *56*, 15658

(28) Zhuang, J.; Chou, L.-Y.; Sneed, B. T.; Cao, Y.; Hu, P.; Feng, L.; Tsung, C.-K. Surfactant-Mediated Conformal Overgrowth of Core-Shell Metal-Organic Framework Materials with Mismatched Topologies. *Small,* **2015**, *41*, 5551

(29) Ren, J.; Musyoka, N. M.; Langmi, H. W.; North, B. C.; Mathe, M.; Kang, X. Fabrication of core-shell MIL-101(Cr)@UiO-66(Zr) nanocrystals for hydrogen storage. *Int. J. Hydrogen Energy.,* **2014**, *39*, 14912

(30) Guo, C.; Guo, J.; Zhang, Y.; Wang, D.; Zhang, L.; Guo, Y.; Ma, W.; Wang, J. Synthesis of core-shell ZIF-67@Co-MOF-74 catalyst with controllable shell thickness and enhanced photocatalytic activity for visible light-driven water oxidation. *CrystEngComm,* **2018**, *20*, 7659

(31) Zhu, G.; Graver, R.; Emdadi, L.; Liu, B.; Choi, K. Y.; Liu, D. Synthesis of zeolite@metal-organic framework core-shell particles as bifunctional catalysts. *RSC Adv.,* **2014**, *4*, 30673

(32) Yang, X.; Yuan, S.; Zou, L.; Drake, H.; Zhang, Y.; Qin, J.; Alsalme, A.; Zhou, H.-C. One-Step Synthesis of Hybrid Core-Shell Metal-Organic Frameworks. *Angew., Chem. Int. Ed.,* **2018**, *57*, 3927

(33) DeCoste, J. B.; Peterson, G. W.; Jasuja, H.; Glover, T. G.; Huang, Y.-g.; Walton, K. S. Stability and degradation mechanisms of metal-organic frameworks containing the $Zr_6O_4(OH)_4$ secondary building unit. *J. Mater. Chem. A.,* **2013**, *1*, 5642

(34) Wu, h.; Yildirim, T.; Zhou, W. Exceptional Mechanical Stability of Highly Porous Zirconium Metal-Organic Framework UiO-66 and Its Important Implications. *J. Phys. Chem. Lett.,* **2013**, *4*, 925

(35) Cavka, J. H.; Jakobsen, S.; Olsbye, U.; Guillou, N.; Lamberti, C.; Bordiga, S.; Lillerud, K. P A New Zirconium Inorganic Building Brick Forming Metal Organic Frameworks with Exceptional Stability. *J. Am. Chem. Soc.,* **2008**, *130*, 13850

(36) Zhao, Y.; Zhang, Q.; Li, Y.; Zhang, R.; Lu, G. Large-Scale Synthesis of Monodisperse UiO-66 Crystals with Tunable Sizes and Missing Linker Defects *via* Acid/Base Co-Modulation. *ACS Appl. Mater. Interfaces.,* **2017**, *9*, 15079

(37) Park, J. H.; Choi, K. M.; Lee, D. K.; Moon, B. C.; Shin, S. R.; Song, M.-K.; Kang, J. K. Encapsulation of redox polysulphides *via* chemical interaction with nitrogen atoms in the organic linkers of metal-organic framework nanocrystals. *Sci. Rep.,* **2016**, *6*, 25555

(38) Wang, J.; Wan, J.; Ma, Y.; Wang, Y.; Pu, M.; Guan, Z. Metal-organic frameworks MIL-88A with suitable synthesis conditions and optimal dosage for effective catalytic degradation of Orange G through persulfate activation. *RSC Adv.,* **2016**, *6*, 112502

(39) Wei, Y.-S.; Zhang, M.; Liao, P.-Q.; Lin, R.-B.; Li, T.-Y.; Shao, G.; Zhang, J.-P.; Chen, X.-M. Coordination templated [2+2+2] cyclotrimerization in a porous coordination framework. *Nat. Comm.,* **2015**, *6*, 8348

(40) Qian, Y.; Cavanaugh, J.; Khan, I. A.; Wang, X.; Peng, Y.; Hu, Z.; Wang, Y.; Zhao, D. Fe/Fe_3C/N-Doped Carbon Materials from Metal-Organic Framework Composites as Highly Efficient Oxygen Reduction Reaction Electrocatalysts. *ChemPlusChem,* **2016**, *81*, 718

(41) Wang, Y.; Lü, Y.; Zhan, W.; Xie, Z.; Kuang, Q.; Zheng, L.; Synthesis of porous Cu_2O/CuO cages using Cu-based metal-organic frameworks as templates and their gas-sensing properties. *J. Mater. Chem. A,* **2015**, *3*, 12796

(42) Furukawa, H.; Cordova, K. E.; O'Keeffe, M.; Yaghi, O. M. The Chemistry and Applications of Metal-Organic Frameworks. *Science,* **2013**, *341*, 1230444

(43) Serre, C.; Mellot-Draznieks, C.; Surblé, S.; Audebrand, N.; Filinchuk, Y.; Férey, G. Role of Solvent-Host Interactions That Lead to Very Large Swelling of Hybrid Frameworks. *Science*, **2007**, , 1828

Acknowledgements

First and foremost, I grateful thank to my advisor Prof. Hoi Ri Moon who support whole my graduation of master's degree. Without her thoughtful encouraging, careful supervision and guidance, this thesis would not have been possible. She is my best mentor ever I met. It was a great blessing and glory to meet her. I'm proud to be her student.

I am thanks for our lab member, Jin Yeong Kim, Jae Hwa Lee, Sungeun Jeoung, Junsu Ha, Kyunghwan Kim, Jaehui Kim, and previous Ji Yun Kim, Byoungnam Moon, Kyung Joo Lee, In Tae Ju, Jeong Min Hwang, and Songho Lee. Without their support, I couldn't achieve my degree. Thanks for giving me enthusiasm for my research and graduate school life. My master's course was happy because of you guys. And I also thank for our all ULECA friends who made my pleasant college life. Also, I am appreciated for Oh Min Kwon and professor Jihan Kim at KAIST for simulation and deep discussion about MOF-on-MOF core-shell

More than everything, I always thanks to our family for supporting me fully and for believing and leading me with unconditional love and support. With their encouragement and unwavering support, I can finish my study.

In addition, I appreciate to committee members of my degree, Professor Myung Soo Lah at UNIST and Professor Min Kim at Chungbuk National University for spending time for evaluation and attending my research presentation. Their sincere advice offered during my defense is invaluable. I always keep in mind.